https://doi.org/10.1016/j.combustflame.2022.112085

Numerical investigation on reacting shock-bubble interaction at a low Mach limit

E Fan[a], Jiaao Hao[b], Ben Guan[c], Chih-yung Wen[b], Lisong Shi[b,*].

[a] *Department of Mechanical Engineering, The Hong Kong Polytechnic University, Kowloon, Hong Kong*

[b] *Department of Aeronautical and Aviation Engineering, The Hong Kong Polytechnic University, Kowloon, Hong Kong*

[c] *College of Aerospace and Civil Engineering, Harbin Engineering University, Harbin 150001, China*

[*] Corresponding author. *E-mail address:* ls.shi@connect.polyu.hk (L. Shi).

Abstract

We investigate the deflagration combustion in the reacting shock-bubble interaction at $M = 1.34$ using a novel adaptive mesh refinement combustion solver with comprehensive H_2/O_2 chemistry. The numerical results are compared with an experiment by Haehn et al. [1]. The Richtmyer-Meshkov instability dominates the shock-bubble interaction, and the shock focusing in the heavy bubble induces ignition. By following the initial experimental setup published by Haehn et al. [1] and adopting the axisymmetric assumption, we successfully reproduce most of the flow features observed in the experiment both qualitatively and quantitatively, including the bubble morphology evolution and the corresponding chemiluminescence images. The fuel consumption rate is nonmonotonic because of unsteady flame propagation, and it also depends on interfacial instabilities. The deflagration waves increase transverse bubble diameter, mildly decrease the total vorticity, and promote mixing by more than 150% because of the thermal effects. The mixing promotion is approximately 88% related to the diffusivity and 12% related to other mechanisms after ignition. A new shock focusing mechanism is observed due to the secondary refracted shock. During shock focusing, Mach reflection occurs and transits from the bifurcated type to the single type. This transition causes two ignitions: the first occurs in the spiral hot spot entrained by the jet vortex, and the second arises from the hot spot caused by the triple point collision. After the second ignition, the newborn flame is a deflagration at the beginning but is unstable and tends to transit to a detonation as a consequence of shock-flame interactions. Nevertheless, the deflagration-to-detonation transition fails, and the stable combustion mode is deflagration.

Keywords: reacting shock-bubble interaction (RSBI); Richtmyer-Meshkov instability (RMI); adaptive mesh refinement (AMR); shock-induced flame; Mach reflection transition; shock-flame interaction.

1. Introduction

The Richtmyer-Meshkov instability (RMI) occurs when a shock propagates through an inhomogeneous mixture; a classical configuration for this phenomenon is a perturbed interface that separates two different fluids accelerated by a shock. The resulting flow fields involve perturbation growth [2], vorticity deposition and transportation [3], and turbulent mixing and transition [4]. This phenomenon is named after Richtmyer because of his theoretical work on the impulsively accelerated interface [5] and Meshkov, who first experimentally validated the former's work [6]. The Kelvin-Helmholtz instability (KHI) always accompanies RMI and acts secondarily.

The classical shock-bubble interaction (SBI) considers a canonical problem that occurs when a planar shock interacts with a spherical gaseous inhomogeneity, which leads to shock refraction and reflection, vorticity generation and transportation, and turbulence [7]. Hereafter, it will be referred to as the inert shock-bubble interaction (ISBI) to differentiate it from its reactive counterpart. Depending on the densities of the bubble gas and the ambient atmosphere, two scenarios arise and are always described using the Atwood number. The Atwood number measures the ratio of the densities and is defined as $At = (\rho_2 - \rho_1)/(\rho_1 + \rho_2)$, where subscript 1 or 2 represents the properties of the ambient gas or the bubble gas, respectively. For the positive (or negative) Atwood case, the refracted shocks travel slower (or faster) than the incident shock and gradually converge (or diverge), and the reflected waves are compression (or rarefaction) waves. Researchers also refer to these two scenarios as the *heavy* and *light* bubble cases, respectively.

Extensive experiments were carried out on the ISBI. Hass and Sturtevant [8] studied ISBI using both cylindrical and spherical bubbles and applied a finite-amplitude wave model to study the mechanism related to turbulence and mixing enhancement. To investigate the mixing that occurs during ISBI, Jacobs [9] utilized a laminar jet to generate cylindrical inhomogeneity and measured the species distribution using planar laser-induced fluorescence (PLIF). Tomkins et al. [10] revisited the mixing problem for a heavy ISBI using the quantitative PLIF method and obtained the instant mixing rate for the first time. The mixing is dominated by the primary RM instability and is characterized by two stages separated by the emergence of secondary KH instability. The shock focusing phenomenon (SFP) occurs in the heavy bubble case, and it represents the collision of the curved incident shocks and refracted shocks near the downstream bubble pole and produces intense temperature and pressure

jumps and additional vorticity deposition [8,11]. SFP is not observed at the downstream pole in the light bubble case as the refracted shock is divergent. For a comprehensive summary of the ISBI studies, please refer to Ranjan et al. [7].

The reacting shock-bubble interaction (RSBI) is a type of reacting RMI phenomenon that occurs in inertial confinement fusion, scramjet engines, and supernova explosions. RMI frequently accompanies reactions, but studies of reactive RMI are limited. In 2012, Haehn et al. [1] reported a *first-of-its-kind* RSBI experiment concerning a heavy premixed combustible gas bubble. This study was of great significance, as it demonstrated for the first time that an isolated spherical mixture could be ignited by shock focusing alone. Extensive experimental results were also reported in Ref. [12,13]. This experiment was later studied in several numerical works [14–17]. However, the agreement was partially satisfactory. In this paper, we numerically reproduce and investigate the low Mach number limit case (M = 1.34) by following Haehn et al.'s experimental setup.

The details of this experimental setup, which is used to study ignition and combustion by the SFP in the RSBI, are listed in Table 1 and described as follows. The experiment was performed in a vertical shock tube at the Wisconsin Shock Tube Laboratory and the incident shock Mach number M ranged from 1.34 to 2.83. The surrounding gas was pure N_2, and the bubble mixture composition was X (H_2:O_2:Xe) = 2:1:3.76 for the reactive case and X (O_2:Xe) = 51:49 for the inert case, with the corresponding Atwood numbers close to 0.473 and 0.484, respectively. The bubble was designed to be spherical and free-falling before the shock impaction, but initial interfacial perturbations still existed, such as non-sphericity with eccentricity e. The bubble morphology was recorded using the planar Mie scattering method, and combustion was diagnosed using the chemiluminescence method. Two limiting combustion phenomena, which depend on the incident shock strength, were found. In the low Mach number limiting case (M = 1.34, 1.65, and 2.01), ignition occurred at a single location near the shock-focusing point, and the combustion zone depicted by the chemiluminescence was triangular. The propagation speed of the reaction front was evaluated to be less than 100 m/s. In the high Mach number limiting case (M = 2.83), the combustion signals were oblate, which implied an earlier ignition and a much larger propagation speed for the reaction front and was dramatically different from the low Mach number counterpart. Moreover, the history of the transverse bubble diameter (TBD) was barely affected by combustion in the case of a low Mach number, while the combustion greatly increased the TBD value in the case of a high Mach number.

Table 1. The setup and combustion type in Haehn et al.'s experiments [1] and related numerical works

	Unshocked States	Bubble shape	Shock Mach number, M	Detonation Initiation	Grid size Δ_{min} (μm)
Haehn et al.'s experiment (2012)[1,12,13]	T_1 = 295 K, p_1 = 1.00 atm.	Nearly spherical, with eccentricity e = 0.26–0.44	1.34, 1.65, 2.01, 2.83	Uncertain	Not applicable
Diegelmann et al. (2016) [14]	T_1 = 350 K, p_1 = 0.25, 0.50, 0.75 atm.	2D simulation, cylindrical bubble	2.30	Yes	59
Diegelmann et al. (2016) [15]	T_1 = 350 K, p_1 = 0.50 atm.	2D simulation, cylindrical bubble	2.13, 2.19, 2.30, 2.50, 2.90	Yes	59
Diegelmann et al. (2017) [16]	T_1 = 295 K, p_1 = 1.00 atm.	3D simulation, 1/4 of the spherical bubble	2.83	Yes	125
Sidharth GS & Graham V Candler (2017) [17]	T_1 = 295, 368.75 K, p_1 = 1.00, 1.25 atm.	3D simulation, 1/4 of the spherical bubble	2.83	Yes	250

These results indicate two distinct flame phenomena. Nevertheless, as ignition and combustion occurred on a microsecond scale, limited combustion details were revealed by the experiment. On the other hand, numerical simulations may complement the experiment. To the authors' knowledge, four numerical studies [14–17] were conducted to explain the experimental observations, but none of them reproduced the experimental data faithfully. Moreover, distinct deviations in initial setups exist between the experiment by Haehn et al. [1] and the four abovementioned simulations, as shown in Table 1. These include the incident Mach number M, the initial temperature T_1, and the initial pressure p_1, which affect the ignition delay time (IDT). Also, the 2D cylindrical bubbles and 3D spherical bubbles create different shock focusing strengths and, hence, different ignition mechanisms [18,19]. Additionally, the detonation predictions in these numerical studies lacked rigorous grid-convergence proof. As numerous detonation simulations [20–24] have clearly indicated that inadequate grids may lead to spurious detonation waves, it is necessary to conduct a proper grid-convergence study before drawing any conclusions. Oran et al. [20] showed that the under-resolving grids produced spurious weak transverse waves and affected the detonation cell sizes and regularity. Mahmoudi and Mazaheri [23] performed systematic grid resolution studies and concluded that at least 50 cells per half reaction length were required for the physical prediction of regular cell structures. Despite the various grid convergence tests in Ref. [14–17], their tests did not directly check the importance of the grid resolution on the flame structure, which may affect the final combustion configurations, according to Oran and Gamezo [25].

The present numerical study reproduces and complements the experiment by Haehn et al. [1] and Haehn [13] at the low Mach number by following most of the experimental setup for the first time. A novel adaptive mesh refinement (AMR) compressible reactive solver is used. The numerical results indicate that the combustion mode

at M = 1.34 is deflagration instead of detonation which was not clearly reported in the experiment. Our analyses focus on the time-space evolution of RSBI, reproduction of the experimental Mie scattering and chemiluminescence results, and evaluating the effects of combustion in terms of vorticity and mixing. Special emphasis is given to the igniting process, including the shock focusing, the Mach reflection transition, and how the wave structures lead to two ignitions and influence the failure of the deflagration-to-detonation transition (DDT). These wave structures for ignition are smaller than 1 mm and have not been reported before. As our first step for numerical RSBI studies with high resolution, this work only surveys the M = 1.34 case [13]. Parametric studies related to incident shock strength and initial uncertainties will be conducted in the future.

We structure the present study as follows: Section 2 outlines the governing equations, AMR method, and other numerical details. Section 3 describes the computational setup, validates the current AMR solver, and presents a rigorous grid-convergence study in terms of flame structures. Section 4.1 presents and discusses the time-space evolutions of ISBI and RSBI as well as the comparison between this simulation and experiment in terms of the TBD history, bubble morphology, and chemiluminescence. Section 4.2 analyzes the effects of combustion on vorticity generation and mixing behavior. Section 4.3 discusses the Mach reflection transition and the formation of two hot spots. Section 4.4 demonstrates the occurrences of two ignitions, flame acceleration due to two-dimensional wave structures, and the failure of DDT. Section 5 concludes with key findings.

2. Numerical model

2.1 Governing equations

The compressible reactive multi-component Navier-Stokes equations are used to model the reactive compressible flows in this work. In a two-dimensional Cartesian coordinate system, the governing equations with n_s species can be written as

$$\frac{\partial \mathbf{U}}{\partial t}+\frac{\partial \mathbf{F}}{\partial x}+\frac{1}{r}\frac{\partial (r\mathbf{G})}{\partial y}=\frac{\partial \mathbf{F}_{\mathrm{v}}}{\partial x}+\frac{1}{r}\frac{\partial (r\mathbf{G}_{\mathrm{v}})}{\partial y}+\mathbf{S}_{\mathrm{c}}+\Psi_{\mathrm{a}}\mathbf{S}_{\mathrm{a}} \tag{1}$$

where $\boldsymbol{U}$ is the conservative variable vector,

$$\mathbf{U}=\left[\rho_1,...,\rho_{n_s},\rho u,\rho v,E\right]^{\mathrm{T}} \tag{2}$$

and $\boldsymbol{F}$ and $\boldsymbol{G}$ are the inviscid fluxes, which are given by

$$\mathbf{F}=\left[\rho_1 u,...,\rho_{n_s} u,\rho u^2+p,\rho uv,(E+p)u\right]^{\mathrm{T}} \tag{3}$$

$$\mathbf{G}=\left[\rho_1 v,...,\rho_{n_s} v,\rho uv,\rho v^2+p,(E+p)v\right]^{\mathrm{T}} \tag{4}$$

The viscous fluxes $\boldsymbol{F}_{\mathrm{v}}$ and $\boldsymbol{G}_{\mathrm{v}}$ are expressed in the following forms:

$$\mathbf{F}_{\mathrm{v}} = \left[-J_{1,x}, ..., -J_{n_s,x}, \tau_{xx}, \tau_{xy}, u\tau_{xx} + v\tau_{xy} - q_x - \sum_{i=1}^{n_s} J_{i,x} h_i \right]^{\mathrm{T}} \tag{5}$$

$$\mathbf{G}_{\mathrm{v}} = \left[-J_{1,y}, ..., -J_{n_s,y}, \tau_{xy}, \tau_{yy}, u\tau_{xy} + v\tau_{yy} - q_y - \sum_{i=1}^{n_s} J_{i,y} h_i \right]^{\mathrm{T}} \tag{6}$$

$\boldsymbol{S}_{\mathrm{c}}$ and $\boldsymbol{S}_{\mathrm{a}}$ are the source terms that arise from the chemical reactions and the assumption of axisymmetric flow, respectively. They are defined as

$$\mathbf{S}_{\mathrm{c}} = [\dot{\omega}_1, ..., \dot{\omega}_{n_s}, 0, 0, 0]^{\mathrm{T}} \tag{7}$$

$$\mathbf{S}_{\mathrm{a}} = [0, ..., 0, 0, p - \frac{2\mu v}{y} - \frac{2}{3}\mu(\frac{\partial u}{\partial x} + \frac{\partial v}{\partial y} + \frac{v}{y}), 0]^{\mathrm{T}} \tag{8}$$

In these expressions, ρ_{i} ($i = 1 - n_{\mathrm{s}}$) is the species density; ρ is the total density of the mixture; u and v are the bulk velocity components; p is the pressure; E is the total energy per unit volume of the mixture; $J_{i,x}$ and $J_{i,y}$ are the species diffusion terms in the x and y directions, respectively; τ_{ij} are the viscous stress components; q_x and q_y are the heat conduction terms in the x and y directions, respectively; h_i is the species enthalpy; $\dot{\omega}_i$ is the chemical mass production term of each species; and μ is the viscosity of the mixture. For two-dimensional planar flow $r = 1$ and $\Psi_{\mathrm{a}} = 0$, while for axisymmetric flow $r = y$ and $\Psi_{\mathrm{a}} = 1$.

The diffusion terms of species i are defined as

$$J_{i,x} = -\rho \left(D_i \frac{\partial Y_s}{\partial x} - Y_i \sum_{m=1}^{n_s} D_m \frac{\partial Y_m}{\partial x} \right) \tag{9}$$

$$J_{i,y} = -\rho \left(D_i \frac{\partial Y_s}{\partial y} - Y_i \sum_{m=1}^{n_s} D_m \frac{\partial Y_m}{\partial y} \right) \tag{10}$$

where D_i is the species diffusion coefficient and Y_i is the species mass fraction.

Following Stokes' hypothesis, the bulk viscosity effect is neglected, and the viscous stresses can be written as

$$\tau_{xx} = \frac{2}{3}\mu \left(2\frac{\partial u}{\partial x} - \frac{\partial v}{\partial y} - \frac{\Psi_a v}{y} \right) \tag{11}$$

$$\tau_{yy} = \frac{2}{3}\mu \left(2\frac{\partial v}{\partial y} - \frac{\partial u}{\partial x} - \frac{\Psi_a v}{y} \right) \tag{12}$$

$$\tau_{xy} = \tau_{yx} = \mu(\frac{\partial u}{\partial y} + \frac{\partial v}{\partial x}) \tag{13}$$

The thermal conduction term is modeled according to the Fourier law,

$$q_x = -\kappa \frac{\partial T}{\partial x} \tag{14}$$

$$q_y = -\kappa \frac{\partial T}{\partial y} \tag{15}$$

where κ is the thermal conductivity of the mixture. Detailed models are presented in Sections A.2 to A.4.

2.2 Numerical methods

We extend a novel open-source cell-based AMR framework, ECOGEN [26], to solve the compressible multi-component reacting flow. Schmidmayer et al. [26] illustrated its ability to predict bubble collapse, shock-droplet interaction, droplet impingement, and shock-bubble interaction. This framework is written in C++ and is easy to extend. It supports dynamic load balancing in parallel computation using the message passing interface and is independent of any other AMR package. In this section, we briefly describe this AMR method and the numerical schemes used to solve the governing equations. For more information, please refer to Schmidmayer et al. [26].

The dual-tree AMR method in ECOGEN [26] is similar to the pioneering cell-based fully threaded tree (FTT) AMR method introduced by Khokhlov et al. [27]. In addition to the cell tree, ECOGEN builds the face tree to store the connectivity. The classical FTT method is criticized for the traffic problem when parallelly addressing the surrounding cells, especially for flux computation or the construction of high-order schemes. In ECOGEN, this traffic problem is eliminated by the novel face tree. The cell neighborship is indirectly provided by the face-tree structure and the cell-face relationship which is similar to the general unstructured grids; each face holds pointers to the "right" and "left" cells. Compared with the FTT method, the extra face tree causes a higher memory load, and the ratio of the geometrical memory load for these two methods is 2.53. When considering the overall memory load consisting of the geometrical and physical variables, however, the ratio is only 2.33 for the single-phase Euler equations [28] and 1.87 for the 10-species hydrogen combustion case in this work.

The grid is halved during each refinement from the root level (or 0^{th} level) to the highest level (or L^{th} level). The grid size on the q^{th} level is $dx_q = 2^{-q} dx_0$, where dx_0 represents the grid size on the root level. The efficiency of this AMR method depends on the specific interleaving time integration method: if the q^{th} level cells advance one step, then the $(q+1)^{\text{th}}$ level cells advance two steps. The global time step Δt_0 is determined on the highest level by the CFL condition:

$$\Delta t_0 = cfl \times 2^L \frac{\min(dx_L, dy_L)}{\max(|u + a|)} \tag{16}$$

where a is the sound speed, and the time step on the q^{th} level is $(\Delta t)_q = 2^{-q} \Delta t_0$.

The grid refinement is controlled by a refinement indicator $0 \le \xi \le 1$ which is evaluated and stored in each cell. On the cell-tree structure, each cell is targeted as either the split cell or the leaf cell depending on whether it can be further refined or not. For the leaf cell when $\xi > \xi_{\text{split}}$, the cell must be split; for the split cell when $\xi < \xi_{\text{join}}$, the cell can be joint. To assure smooth grid transition [26,27], the difference in levels between two neighboring cells must be smaller than 2. The refinement indicator ξ is evaluated in two steps. In the first step, for each computational cell, ξ is determined by the significant gradients:

$$\xi = \begin{cases} 1 & \text{, when } \dfrac{\left|Q_{i,neighbor} - Q_i\right|}{\min(Q_{i,neighbor}, Q_i)} > \varepsilon \\ 0 & \text{, otherwise} \end{cases} \tag{17}$$

Here, Q represents the physical properties, including the p, ρ, T, velocity magnitude, and mass fraction. In the second step, a diffusive equation governs the smoothing of ξ

$$\frac{\delta \xi}{\delta \tilde{t}} = K \nabla^2 \xi \tag{18}$$

where $\tilde{t}$ is a fictitious diffusive time step, and $K = 2^{-2l} \max(dx_0, dy_0)^2$ is a diffusive coefficient that assures smooth AMR grid transition. Following Ref. [26,27], in this study, $\varepsilon = 0.08$, $\xi_{\text{split}} = 0.02$, and $\xi_{\text{join}} = 0.11$.

To further promote computational efficiency in this combustion simulation, we design a special AMR strategy based on the empirical threshold of the ignition/flame temperature $T_{\text{et}} = 900$ K to refine the hydrodynamic and chemical discontinuities separately:

$$L = \begin{cases} L_{\text{hydro}} \\ L_{\text{chem}} \end{cases}, Q = \begin{cases} p, \rho, T, \sqrt{u^2 + v^2} & \text{,when } T < T_{\text{et}} \\ p, \rho, T, \sqrt{u^2 + v^2}, Y_{OH} & \text{,when } T \ge T_{\text{et}} \end{cases} \tag{19}$$

Here, L_{hydro} and L_{chem} represent the highest refined levels for hydrodynamic and chemical discontinuities, respectively, and L_{hydro} is always smaller than L_{chem}.

Governing equation integration is performed in a face-by-face manner. By iterating over the leaf faces on the refined level, both the inviscid and viscous fluxes are evaluated and added to the "left" and "right" cells. Each parental cell is conservatively evaluated by its offspring. The inviscid fluxes are estimated using a Godunov-type method when solving the Riemann problems. The multi-component Harten-Lax-van Leer Contact (HLLC) solver [29], which is extended by the monotone upstream-centered schemes for conservation law reconstruction (MUSCL)[30], is implemented to evaluate the inviscid flux. The viscous fluxes are evaluated using a 2nd-order central scheme with skewness correction [31]. The axisymmetric source vector, $\boldsymbol{S}_{\text{a}}$, is simply added to the right-hand side of the governing equation. The chemical source vector, $\boldsymbol{S}_{\text{c}}$, is decoupled from the conservative system

and solved using the CANTERA package [32] with up to 6th-order temporal accuracy. A 2nd-order Runge-Kutta method [33] is employed for temporal integration other than chemical reactions.

3. Computational setup

3.1 Geometric configuration and initial conditions

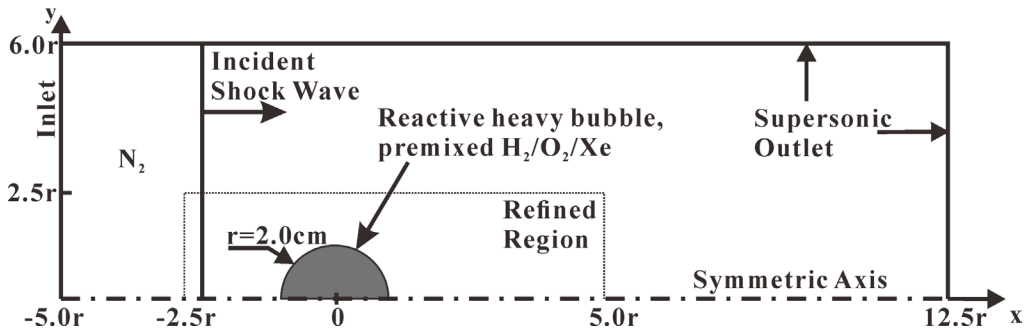

Figure 1. The computational domain of ISBI and RSBI simulations.

We study the inert and reactive SBI within a two-dimensional domain in Figure 1 and use the axisymmetric assumption to reduce the computational load. The left boundary is set as the inlet, the upper and right boundaries are set as the supersonic outlet, and the lower boundary is set as symmetric. Initially, the bubble center is located at (0,0). The bubble and its surrounding N_2 atmosphere are defined by the molar fraction of the bubble mixture, similar to that in Ref. [14]:

$$X_{\text{bubble}} = \frac{1-\tanh\left(\left(\sqrt{x^2+y^2}-r\right)\cdot C\right)}{2} \tag{20}$$

where r = 0.02 m is the nominal bubble radius, $C = 2\times10^5$ m^{-1} and $X_{N2} = 1-X_{\text{bubble}}$. For both inert and reactive SBI simulations, the bubble compositions are $X(H_2{:}O_2{:}Xe) = 2{:}1{:}3.76$, and the chemical source terms are switched off in the inert case. The computational domain is a $17.5r \times 6r$ rectangle. The incident shock wave propagates from the left side of the computational domain, and the post-shock states are set according to the Rankine-Hugoniot relations. We perform a numerical study on the M = 1.34 axisymmetric RSBI problem by exactly following the initial setups in Haehn et al.'s experiment [1]: initially, the pre-shocked states are T_1 = 295 K and p_1 = 1 atm. To further decrease the computational load, once the bubble is ignited and the predicted combustion type is stable, the computational domain moves with some constant speed relative to the laboratory coordinate system to keep the shocked bubble inside the refined region. This is achieved by subtracting the shocked bubble speed calculated using a one-dimensional simulation from the velocity field and was prevalently utilized in other combustion simulations [25,34,35].

3.2 Numerical method validations

3.2.1 High-pressure IDT

In this study, we use the pressure-dependent H_2/O_2 mechanism in Ó Conaire et al. [36] to model combustion at elevated temperatures and pressures during shock focusing. Figure 2 shows the ignition delay time with $X(H_2{:}O_2{:}Ar)$ = 2:1:97 at 33 atm as predicted by several chemical mechanisms and measured in shock tube experiments by Petersen et al. [37]. Comparisons show that our simulation with the Ó Conaire mechanism performs well against the experiments, showing that the Ó Conaire mechanism suits the high-pressure combustion simulation with good accuracy.

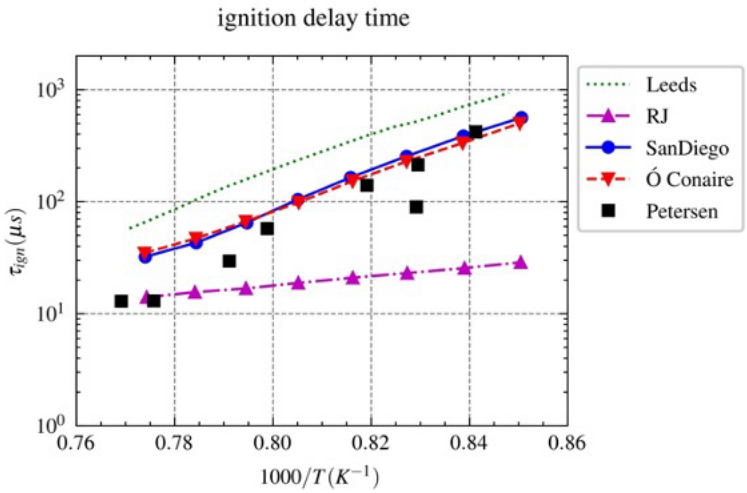

Figure 2. Ignition delay time with $X(H_2{:}O_2{:}Ar)$ = 2:1:97 at 33 atm. Numerical predictions: the Leeds mechanism is from Ref. [38], RJ represents the reduced Jachimowski mechanism from Ref. [39], the San Diego mechanism is from Ref. [40], and the Ó Conaire mechanism is from Ref. [36]. The experimental data are from Petersen et al. [37].

3.2.2 Two-dimensional cylindrical RSBI

We reproduce the M = 2.30 cylindrical RSBI case in Ref. [15] to validate the accuracy of our AMR solver on such problems. Initially, T_1 = 350 K and p_1 = 0.5 atm. Other initial setups and geometrical configurations are presented in Section 3.1. As Ref. [15] evaluated the inviscid fluxes using a 6^{th}-order scheme, we manage to achieve similar results by halving the minimum grid size. L = 3, and in the refined region, dx_0 = 400 μm and dx_L = 50 μm.

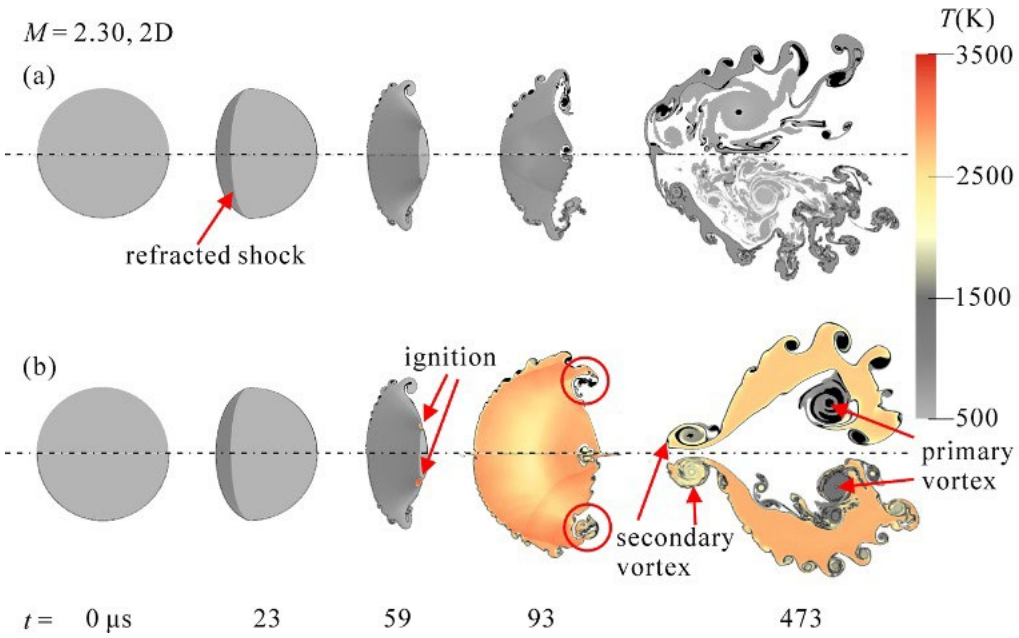

Figure 3. Temperature contour plots of (a) the 2D cylindrical ISBI case and (b) the RSBI case with limiting Y_{Xe} > 0.1. In each subfigure, the upper regions depict the results in this study, and the lower regions depict the results in Ref. [15].

Figure 3 compares the simulated temperature contours of the cylindrical RSBI and ISBI cases at M = 2.30 between this study and Ref. [15]. Until further notice, the thick black/purple lines delineate the iso contour of $Y_{Xe} \in [0.35, 0.55]$, representing the bubble interfaces, and the dash-dotted lines represent the symmetry lines (in the cylindrical case) or the axis (in the axisymmetric case). Comparing our results with those in Ref. [15], the ISBI behaviors are almost the same from 0 to 93 μs. At t = 473 μs, although more small-scale structures are shown in Ref. [15] inside the vortex and on the interface, the bubble head location, position and shape of the primary vortex, and unstable interfacial structures are effectively reproduced in our AMR simulation. For the reactive case, the ignition time and location at 59 μs are nearly the same. At 93 μs and 473 μs, the damping of unstable interfacial structures, heat expansion, and temperature distribution are also similar in both studies. These analyses prove that our numerical method is a reliable tool for RSBI simulations.

3.3 Grid-convergence study

Five cases with different grid setups are tested. Table 2 and Figure 4 present the AMR grid setups around the bubble. In Case 1, dx_0 = 400 μm on the root level. In other cases, the root grids around the downstream pole are specially set with dx_0 = 64 μm to improve the computational efficiency and dynamic load balancing. From Case 2 to Case 5, the L_{chem} increases from 2 to 6, and dx_{min} decreases from 16 to 1 μm.

Table 2. The initial grid setups around the bubble in the grid-convergence study of the RSBI at M = 1.34.

Case ID	minimum dx_0 (μm)	L_{hydro}	L_{chem}	$dx_{\min} = dx_{L_{\text{chem}}}$ (μm)
1	400	3	3	50
2	64	2	2	16
3	64	2	4	4
4	64	2	5	2
5	64	2	6	1

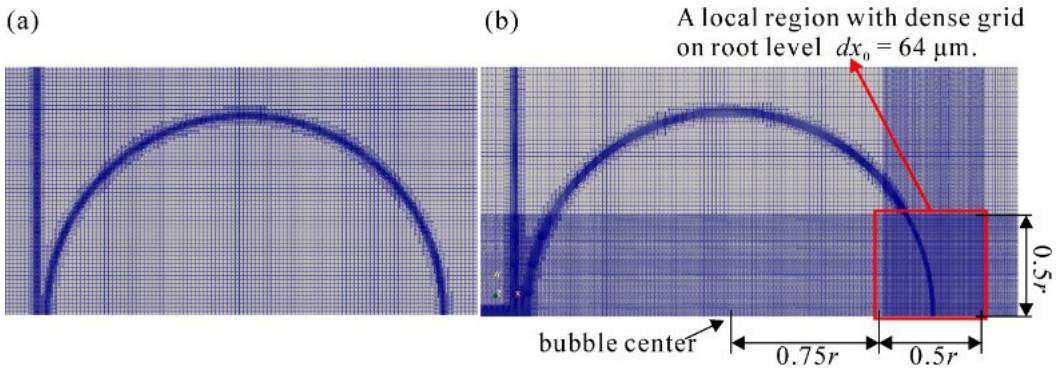

Figure 4. The initial AMR grids around the bubble in the grid-convergence study of the RSBI at M = 1.34. (a) Case 1. (b) Cases 2–5. The root grids in the $0.5r \times 0.5r$ area near the downstream pole are set to dx_0 = 64 μm.

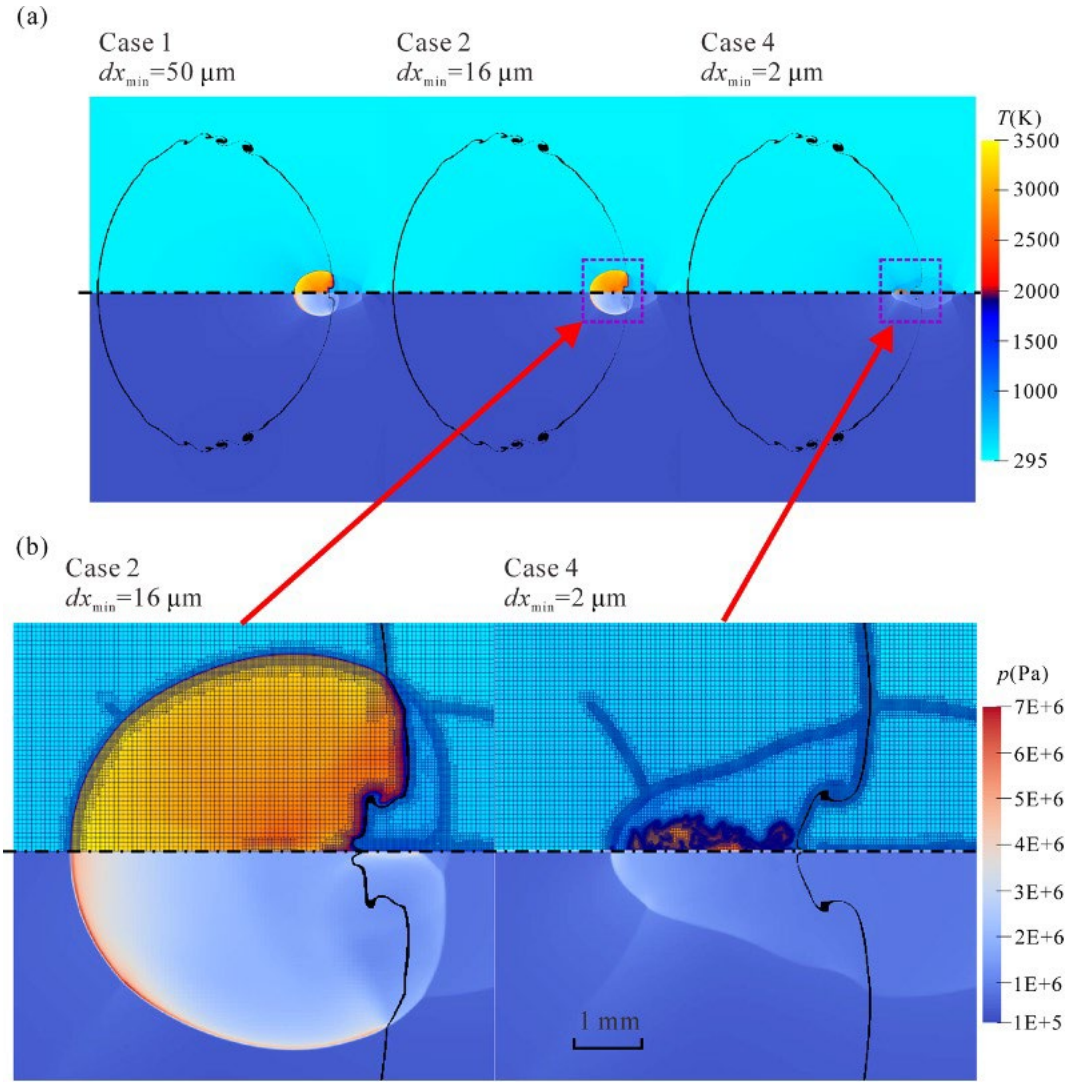

Figure 5. Flow fields for the M = 1.34 RSBI in Cases 1, 2, and 4 at 125 μs. In each subfigure, the upper regions depict temperature contours, and the lower regions depict pressure contours. (a) Global views of the bubble in all 3 cases and (b) detailed views of the flame and grids for only Cases 2 and 4.

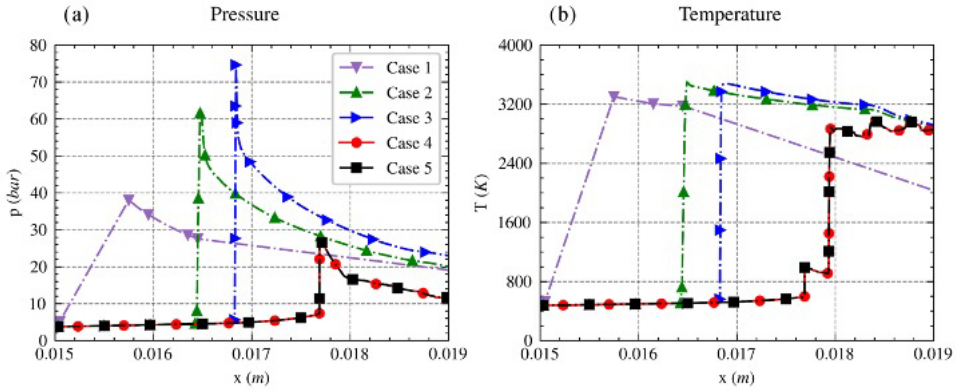

Figure 6. One-dimensional pressure and temperature distributions along the symmetry axis from Cases 1–5 at 125 μs.

Figure 5 depicts the combustion results for the M = 1.34 RSBI at 125 μs in Cases 1, 2, and 4. At this moment, shock focusing ignites the bubble, and the combustion mode is stable. On one hand, both the flames predicted in Cases 1 and 2 are spherical detonation waves; on the other hand, the flame in Case 4 is deflagration with a smaller flame and lower peak pressure when compared with the former cases. Further examination of the one-dimensional flame structures along the symmetry axis in Figure 6 shows that Cases 2 and 3 predict typical detonation waves in which the flame fronts closely attach to the preceding shocks with a large pressure jump, whereas Cases 4 and 5 predict consistent deflagration waves in which the flame fronts are decoupled from the shocks with a mild pressure difference. Therefore, the grids in Case 4 can adequately guarantee grid convergence in this combustion simulation.

The grids for Case 4 in Figure 5(b) clarify the AMR strategy based on T_{et}. The reflected shocks and bubble interfaces are colder than T_{et} and are only refined to the 2nd level (L_{hydro} = 2), while the flame fronts are hotter than T_{et} and become refined to the 5th level (L_{chem} = 5). Using this strategy, the flame fronts and reaction waves are adequately described by the grids ($dx_{L_{chem}}$ = 2 μm), which are nearly one order of magnitude smaller than the grids around the hydrodynamic discontinuities ($dx_{L_{hydro}}$ = 16 μm), and the computational efficiency is higher than that exhibited when treating all discontinuities uniformly.

Therefore, the following discussions and analyses are all based on the results from Case 4. The simulation covers 1708 μs after the incident shock reaches the upstream bubble pole. For reference, the incident wave speed is W_i = 468 m/s, the hydrodynamic time scale is $\tau_H = 2r/W_i$ = 85.4 μs, and the non-dimensional time range $t^* = t/\tau_H$ is from 0 to 20. The time step is limited by a maximum CFL number of 0.3. The minimum time step is approximately 5.80 ns on the root level and 0.18 ns on the highest refined level when shock focusing and ignition occur. All simulations were performed in parallel on 180 cores of the Tianhe supercomputer in Tianjin Supercomputer Center, China, and the computational time for the reactive case was approximately 20 days.

4. Results and discussion

4.1 Spatial and temporal evolutions of ISBI and RSBI

In this section, we present and discuss the temporal and spatial evolutions of ISBI and RSBI as well as the comparison between this simulation and the experiment, including the TBD history, bubble morphology, and chemiluminescence images.

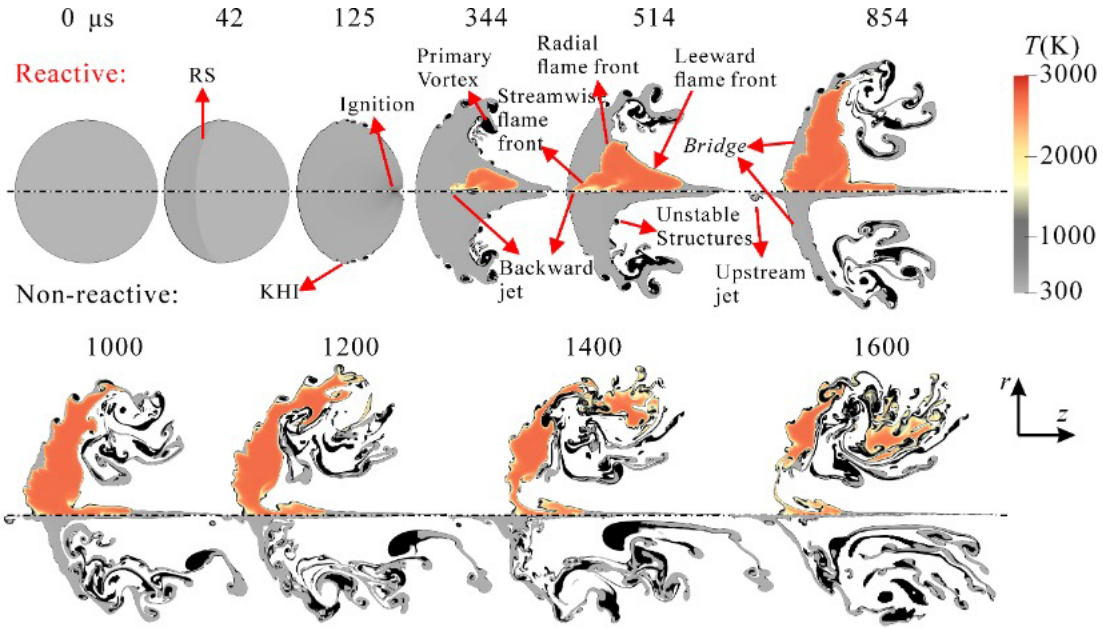

Figure 7. Temperature contours for the RSBI (upper) and ISBI (lower) with limiting $Y_{Xe} > 0.1$. RS: refracted shock, KHI: Kelvin-Helmholtz instability.

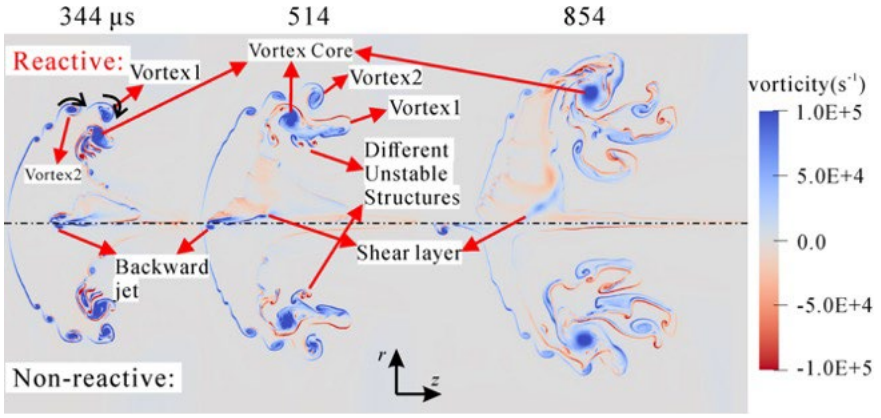

Figure 8. Vorticity contours for the RSBI (upper) and ISBI (lower) from 344 to 854 μs.

Figure 7 presents the instantaneous temperature contours inside the bubble in both the RSBI and ISBI cases and Figure 8 shows their vorticity contours. At $t = 0$ μs, the shock-bubble interaction starts.

We first consider the non-reactive results in Figure 7 and Figure 8. In this shock-heavy-bubble interaction case with $At = 0.48$, at 42 μs, the windward side interface triggers large-scale RMI and gets compressed. The refracted shock (RS) travels slower than the incident shock and is convergent. At 125 μs, the velocity differences across the equatorial interface induce the secondary KHI. Shock focusing of the diffracted waves, which is not visible in this frame, occurs at the rear of the bubble and extrudes the downstream-pole interface inward. At 344 μs, the primary vortex, which is caused by the large-scale RMI, emerges near the equator, and small-scale structures, which are caused by the secondary KHI, appear on the leeward side interface. The vorticity contours in Figure 8 show that

shock focusing induces an obvious backward jet along the symmetry axis, and the jet propagation agrees with the "vortex ring projectile" in Zabusky and Zeng [18]. The backward jet penetrates through the upstream interface (514 μs) and gives birth to an upstream jet (854 μs). From 514 to 1600 μs, the primary vortex grows both in streamwise and transverse directions, and the bubble material gets more distributed. The upstream bubble material connecting the counter-rotating vortices becomes thinner and was referred to as the "bridge" by Tomkins et al. [10].

The sequences in the upper halves of Figure 7 and Figure 8 show the development of the RSBI case. Before 42 μs, the bubble has not yet been ignited, and the inert and reactive flow fields are the same. In Figure 7, at 125 μs, ignition occurs due to shock focusing on the bubble's downstream pole. The flame structures are on a scale of less than 1 mm and are later discussed in Section 4.4. At 344 μs, the flame grows inside the bubble, but the flame fronts have not yet interacted with the interface. The flame continues to expand until 514 μs, and here, we separate the flame fronts into three groups according to the orientations and denote them as the streamwise, radial, or leeward flame fronts. Compared with the ISBI case, the small-scale structures on the leeward side interface are damped by a baroclinic effect due to the pressure gradient and density jump across the flame [34,41], and the bubble tail lies more downstream. From 854 to 1200 μs, the flame gradually consumes the premixtures in the bridge region: the streamwise flame front reaches the upstream interface, and the outermost radial flame front approaches the unburnt primary vortex. Compared with the inert case, the bridge region becomes thicker because of heat expansion, and the upstream jet disappears. After 1000 μs, since the burnt mixtures are lighter, the reacting primary vortex structures are considerably influenced by combustion and are more discrete than the inert ones. Figure 8 shows the head of backward jet in the reactive case, which lies more upstream at 344 μs and slightly more downstream at 514 μs than the inert jet. It also implies that the flame fronts generate extra vorticity inside the bubble, and a shear layer is located near the axis inside the flame.

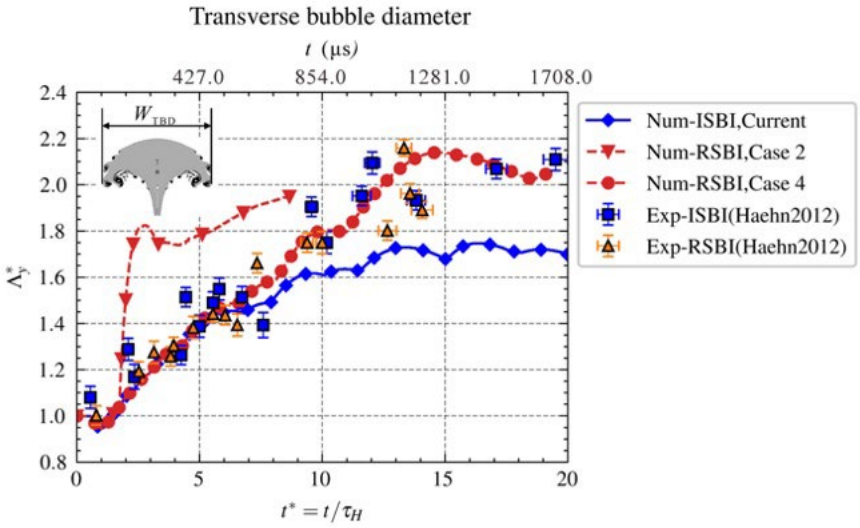

Figure 9. The nondimensional TBD values as a function of nondimensional time in our simulation and Haehn's experiment [13] from 0 to 1708 μs.

Figure 9 plots the nondimensional transverse bubble diameter $\Lambda_y^* = W_{TBD}/2r$ as a function of nondimensional time t^*, in which W_{TBD} is the value of TBD. Most inert and reactive experimental data are effectively predicted by the simulations. Before $0.6\tau_H$, as the incident shock only compresses the windward side interface, the TBD values remain constant. After $0.6\tau_H$, the incident shock reaches the leeward side interface, and the TBD decreases due to the large-scale RMI effects. The TBD value reaches its minimum value at approximately τ_H. After that, the continuing increase is due to the growth of the primary vortex. The plateau at approximately $4\tau_H$, which is seen both experimentally and numerically, can be explained by the unsteady evolution of Vortex1 and Vortex2 from 344 to 514 μs in Figure 8; when the primary vortex rotates clockwise, since the movement of Vortex1 tends to decrease the TBD while the development of Vortex2 tends to increase it, the overall outcome is a plateau at approximately $4\tau_H$. After $4.1\tau_H$, since the spanwise movement of Vortex2 prevails, the TBD value increases. The later trends at $6.5\tau_H$ and $10\tau_H$ can be interpreted similarly. Before $6\tau_H$, both reactive and inert TBD values overlap; after that, the reactive results exceed the inert ones. These excesses can be explained by both the sound waves that originated from combustion which act as pistons and push the interfaces and the burnt mixture which partly converts the case into a shock-lighter-bubble interaction. Since the three-dimensional effect, turbulence and initial perturbations may play important roles in long-term SBI evolution [7,11,42], deviations between the numerical and experimental data grow after $10\tau_H$ [16]. We also plot the TBD history predicted by the Case 2 simulation, and the detonation waves greatly increase the TBD values after $1.7\tau_H$. The overestimation of the experimental data further proves that the detonation obtained on coarse grids is not physical.

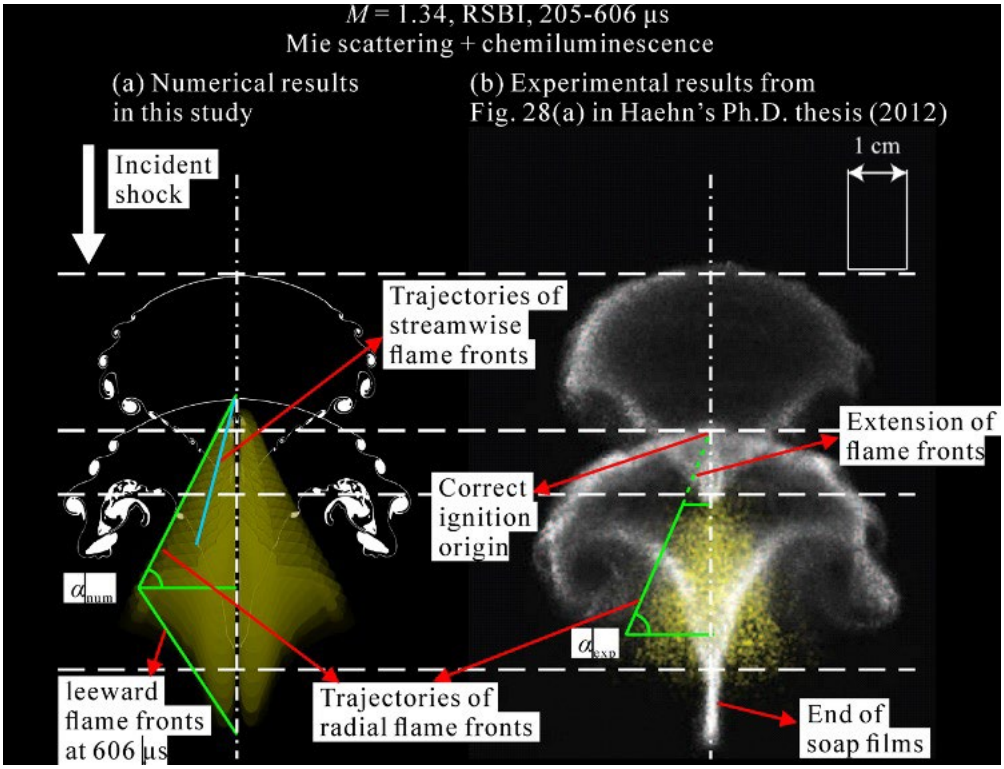

Figure 10. Combined images of the bubble morphology and combustion signals in the RSBI case from 205–606 μs. (a) Our numerical results: the white solid lines represent bubble interfaces, and the yellow region is the superposition of the enhanced OH^* contour. (b) The experimental result from Ref. [13]. The dash-dotted white lines represent the symmetry axis.

Figure 10 shows the combined images of the bubble interfaces (white signals) and flame fronts (yellow signals). The bubble interfaces are experimentally captured by the planar Mie scattering method and numerically plotted as the iso contours of $Y_{Xe} \in [0.35, 0.55]$ instantly at 205 and 409 μs. The flame fronts are experimentally diagnosed by planar chemiluminescence and numerically plotted as suppositions of instant OH^* distributions evenly sampled in the same time range. The numerical OH^* distributions are calculated using the quasi-steady-state assumption [43]. The dashed white lines mark the experimental locations of the bubble heads or tails, and the tails are regarded as the intersection of leeward interfaces instead of the ends of soap films to avoid interference. Since the experiment did not record the vertical locations, the best we can do is to vertically align the numerical and experimental bubble heads at 205 μs and plot the corresponding results at 409 μs. At 205 μs, both the numerical and experimental interfaces consist of a hemisphere on the windward side and a reversed cone on the leeward side, and the corresponding streamwise bubble lengths are almost identical. At 409 μs, both results show obvious primary vortex structures and small-scale unstable KHI structures similarly. Although both the numerical head and tail lie more upstream than the experimental head and tail, the streamwise length scale remains nearly the same. This observation indicates that numerically, the bubble travels less downstream, and the dislocation is

around 0.47 cm. This difference may be caused by the mass of the soap film bubble interface in the experiment. Table 3 shows the relative TBD error from Figure 10. Overall, the relative error of W_{TBD} is less than 9%.

Table 3. Lengths and angles in Figure 10

	t (μs)	exp	num	Relative Error (%)
W_{TBD}	205	5.165 cm	4.704 cm	8.93
	409	6.118 cm	5.835 cm	4.62
α		23.54°	27.45°	15.76
cot α		2.295	1.942	15.41

The flame fronts in Figure 10 are outlined in solid green. In these two-dimensional images, the experimental result is an isosceles trapezoid, while the numerical results consist of a triangle and a reversed triangle. In general, the numerical triangular signal is consistent with the observation by Haehn et al. [1] at the lower Mach number limit. These numerical and experimental signals are explained as the superposition of the streamwise main flow and spanwise flame propagation. The trapezoidal shape in the experimental image may result from the failure to capture early ignition signals, and the correct origin of the flame front shall lie on the intersection of the extended flame fronts (dashed green line) and the symmetry axis (dash-dotted white line). With this correction, the ignition spot coincides with the bubble head at 409 μs, which is precisely reproduced by the simulation. The numerical and experimental inclinations of the flame fronts are denoted as α_{num} and α_{exp}, respectively, and they can be used to evaluate the speed ratio between the flame fronts and the main flow $V_{flame}/V_{mainflow} = \cot \alpha$ [1]. Table 3 also compares these numerical and experimental angles and speed ratios, and the maximum relative error is less than 16%. The hypotenuse of the numerical triangular signature is the trajectories of the radial flame fronts, and the hypotenuse of the reversed triangular signature is the leeward flame front at 606 μs. Since we neglect the soap film in the modeling, the numerical flame fronts are not damped by the water droplets [44,45]; otherwise, better agreements would be achieved as the reversed triangular signals may disappear. Another interesting numerical finding is the trajectory of the streamwise flame fronts marked by the solid cyan line. These flame fronts are entrained by the backward jet. These numerical signals were not identified in the experimental work by Haehn et al. [1] due to the overlap with the radial flame front signals. Considering that the experiments were inevitably influenced by the interfacial perturbations and that the numerical deviations arise from the chemical mechanism and the neglect of the soap film, the unsteady bubble morphology and flame signature are, surprisingly, reproduced both qualitatively and quantitively.

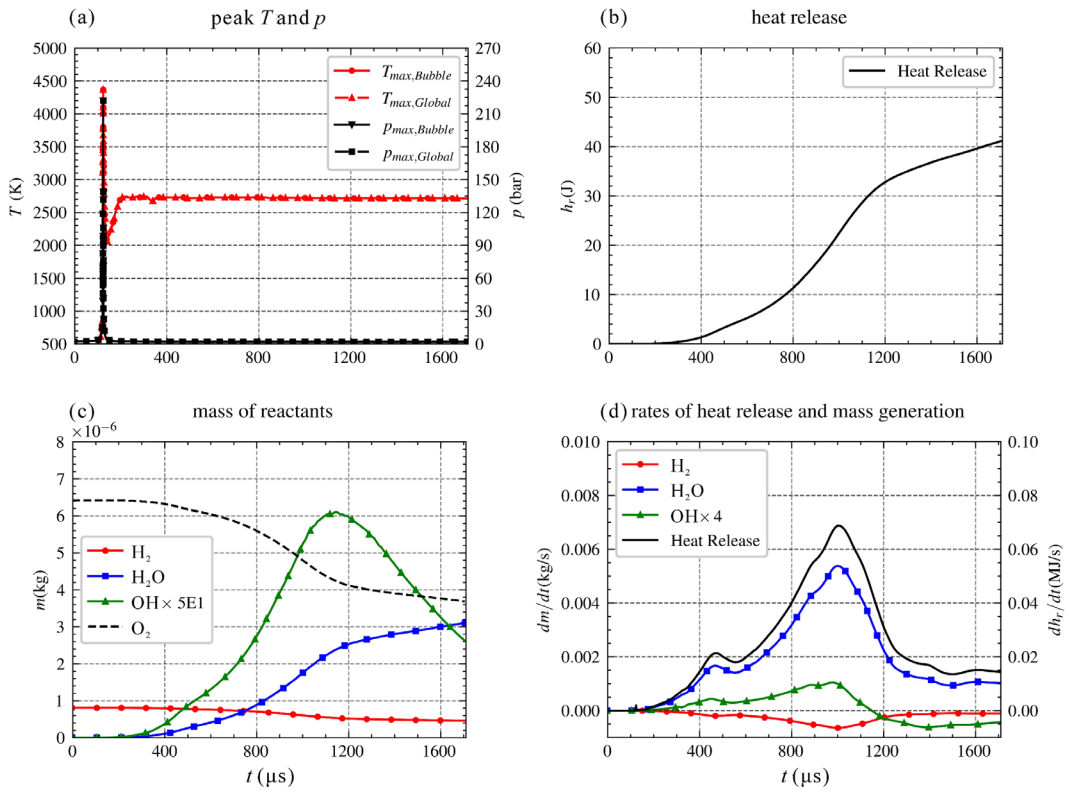

Figure 11. Instantaneous properties from 0 to 1708 μs: (a) peak temperature and pressure in the global flow field and inside the bubble, (b) heat release, (c) mass of some reactants, and (d) rates of heat release and mass generation.

Figure 11 plots the global history of several thermodynamic and chemical properties during the simulation. Most of the time, the location with the maximum thermodynamic states lies inside the bubble. The peaks with $T_{max,bubble}$ = 4400 K and $p_{max,bubble}$ = 223 bar are detected at approximately 122 μs when shock focusing occurs and quickly ignites the bubble. The history of m_{O2} indicates that around 44% of premixtures are burnt at the end of the simulation. The maximum fuel consumption rate is 7.21×10^{-4} kg/s at around 1000 μs, and dm_{H2}/dt is nonmonotonic. Figure 12 presents the Y_{H2} contour and can be used to explain these nonmonotonic behaviors from 400 to 700 μs. During this period, the overall fuel consumption rate is caused by the collective effect of the upstream, radial, and leeward flame fronts. Since the leeward flame fronts arrive at the interface and are no longer accessible to the fresh unburnt premixtures after 470 μs, dm_{H2}/dt decreases despite the contributions from other flame fronts. From 560 to 1000 μs, the radial fronts continue stretching in the bridge region. Considering the axisymmetric configuration, the fuel consumption rate is dominated by radial fronts and continues to increase. After 1000 μs, the bridge region is almost fully burnt, and flame propagates into the primary vortex. Since the flame fronts can only approach unburnt mixtures via the narrow interfacial channels between distributed materials (see Figure 7), the fuel consumption rate decreases, and combustion are suppressed due to interfacial mixing.

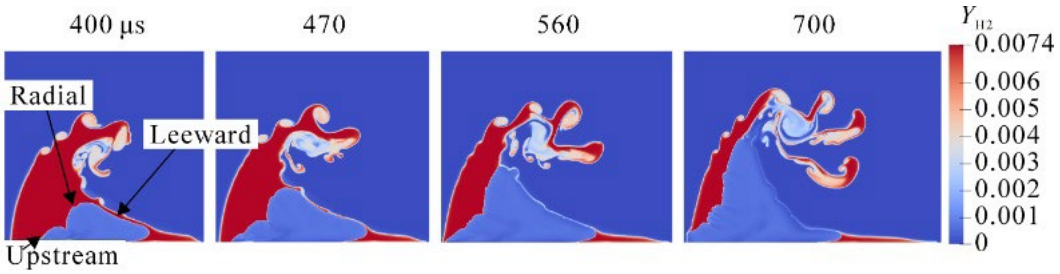

Figure 12. Y_{H2} contours in the RSBI case from 400 to 700 μs.

4.2 Effects of combustion on vorticity and mixing

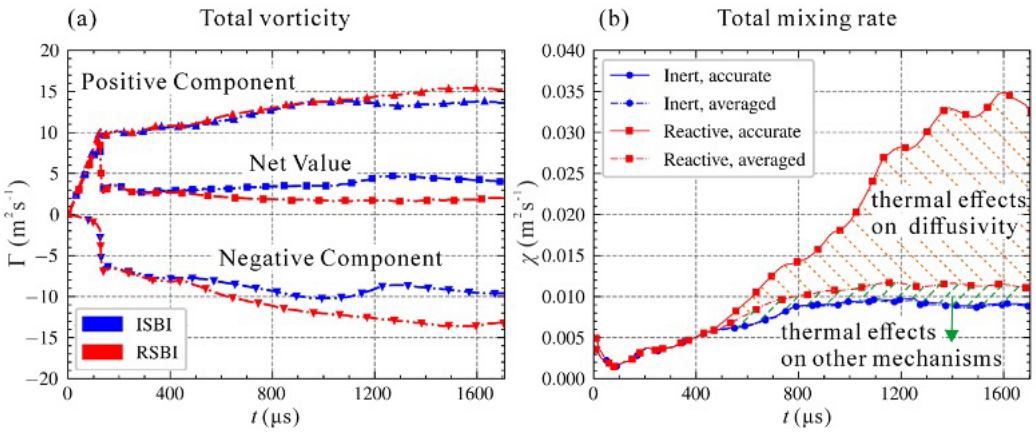

Figure 13. The history of (a) the vorticity and (b) the mixing rate in both the ISBI and RSBI cases.

Figure 13 plots the vorticity and mixing rate in the ISBI and RSBI cases. The total vorticity is defined as $\Gamma = \int \omega dxdy$. To avoid the interference of combustion on the gradients of the reactive species, we examine the mixing behaviors between two inert species, N_2 and Xe, which are initially located either inside or outside the bubble. The mixing rate χ between N_2 and Xe is adopted from Tomkins et al. [10] as

$$\chi = \int D_{\mathrm{Xe,N_2}} \left(\nabla Y_{\mathrm{Xe}} \cdot \nabla Y_{\mathrm{Xe}} \right) dxdy \tag{21}$$

where $D_{\mathrm{Xe,N_2}}$ is the binary molecular diffusivity.

Figure 13 (a) presents the total vorticity along with the positive Γ^+ and negative Γ^- components. For the ISBI case, the net vorticity is always positive. Before 122 μs, the magnitudes of Γ and both components monotonically increase: the magnitude of Γ^+ increases via the primary RMI effects and the magnitude of Γ^- increases via the secondary KHI effects. At 122 μs, the positive components drop slightly, and the magnitude of Γ^- drastically increases because of shock focusing. The net vorticity value also decreases. After 125 μs, the incident shock has already passed through the bubble. Therefore, the magnitudes of Γ^+ and Γ^- grow mildly. After 500 μs, the reactive Γ^- magnitude is larger than that in the inert case as a result of more negative vorticities deposited on the flame

fronts (see Figure 8). The Γ^+ values in both cases almost overlap before 1200 μs, and the reactive one is larger afterward. Overall, before 500 μs, the Γ values in both cases are the same. After that, the Γ of the RSBI case is smaller.

Figure 13 (b) illustrates the history of the mixing rate χ. Tomkins et al. [10] proposed that the mixing rate in a shock-accelerated flow depends on several mechanisms, including the steepening of ∇Y_i through the straining effects and an increase in interfacial area due to the RMI and KHI effects. In this combustion study, apart from the thermal effects caused by the aforementioned two mechanisms, since the combustion drastically changes p and T, another mechanism arises according to Eq. (32), e.g., $D_{\mathrm{Xe,N_2}} = D_{\mathrm{Xe,N_2}}(p,T)$, and we refer to it as the thermal effects due to the diffusivity. To quantitively evaluate the importance of these mechanisms, we compare both the "accurate" and "averaged" mixing rates: the accurate rate is obtained by numerically integrating Eq. (21), whereas the averaged rate is evaluated similarly but uses the averaged diffusivity $\overline{D}_{\mathrm{Xe,N_2}} = D_{\mathrm{Xe,N_2}}(p_1', T_1')$, where p_1' and T_1' are the post-shock pressure and temperature behind the incident shock, respectively. The incident shock fully passes the bubble at approximately 120 μs. Before 120 μs, the inaccuracy of the averaged χ results from the overestimation in $\overline{D}_{\mathrm{Xe,N_2}}$ because the bubble is only partially compressed. After that, the accurate χ in the inert case can be effectively evaluated using $\overline{D}_{\mathrm{Xe,N_2}}$. In the reactive case, the difference between the accurate and averaged χ, which is shaded by the dashed orange lines, represents the contribution related to the thermal effects on diffusivity. In addition, the difference between the reactive averaged χ and inert accurate/averaged χ, which is shaded by the dashed green lines, represents other contributions relevant to the concentration gradient and interfacial area. The inert accurate χ decreases before 90 μs as a result of the shock compression on the windward interface. From 90 to 210 μs, χ increases because of the small-scale interfacial structures caused by secondary KHI. The decrease from 210 to 250 μs can be explained by the competition between different mechanisms [10]: the increase in the interfacial area promotes the mixing rate but also smooths the concentration gradient, and sometimes the overall outcome is a decrease in mixing. After 250 μs, the primary vortex continues to develop and entrain the surrounding N_2, which dominates the increment of χ till 800 μs. The inert mixing rate almost kept the same after 800 μs. The mixing behaviors of both the inert and reactive case before 470 μs are the same. After that, the flame fronts reach interfaces and promote mixing. At 1200 μs, the reactive χ is approximately three folds of the inert one, in which 86% of the growth is related to the diffusivity and 14% is due to other mechanisms. Temporal integration of χ shows that combustion increases overall mixing by approximately 156%, in which 88%

of the growth is related to diffusivity and 12% is due to other mechanisms. Therefore, in this study, combustion significantly promotes mixing in SBI, and the contributions primarily lie in the thermal effects on diffusivity.

4.3 Mach reflection transition in the ISBI

In this section, we analyze the Mach reflection transition process and the formations of two hot spots after shock focusing in the ISBI case. The flow field of interest is as the rectangular region in Figure 5 (a).

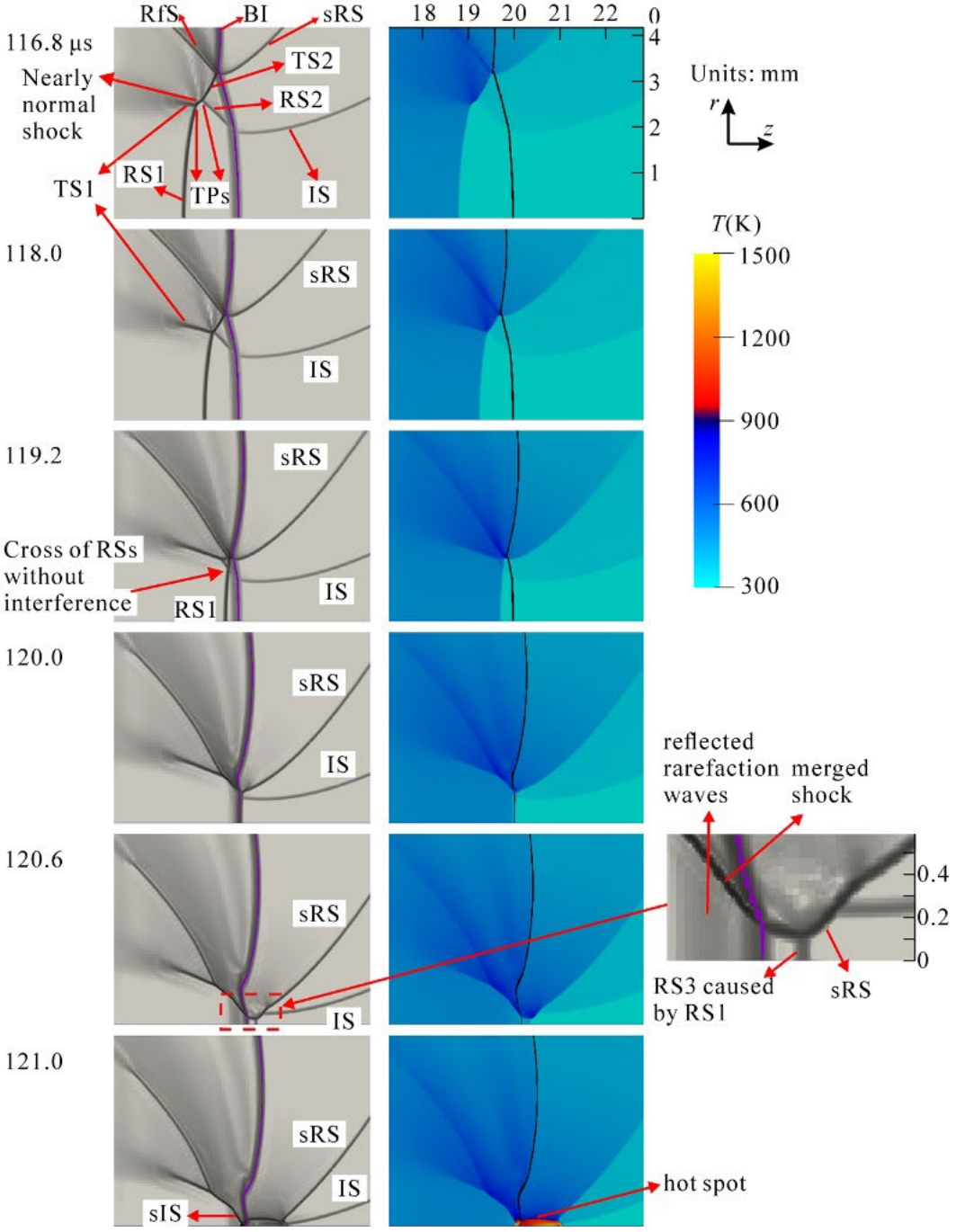

Figure 14. Numerical schlieren and temperature contours near the downstream pole in the ISBI case from 116.8 to 121.0 μs. BI: bubble interface, IS: incident shock, RS1, RS2: refracted shocks, RfS: reflected shock, sIS:

secondary incident shock, sRS: secondary refracted shock, TS1, TS2: transmitted shocks, TPs: triple points. The lower boundary in each frame coincides with the symmetry axis.

Figure 14 demonstrates the shock-focusing process from 116.8 to 121.0 μs in the ISBI case. At 116.8 μs, the curved incident shock (IS) propagates along the leeward side interface toward the symmetry axis. With a positive Atwood number, fast–slow refraction occurs between IS and the bubble interface (BI), which produces a refracted shock (RS2); besides, RS1 is caused by refraction at the windward side interface. A Type II shock-shock interaction, as discussed by Edney [46], occurs between RS1 and RS2, and the outcomes are two triple points (TPs), a nearly normal shock, and two transmitted shocks denoted by TS1 and TS2. Of these two shocklets, TS2 is strong, and TS1 is weak. Slow–fast refraction occurs between TS2 and BI, resulting in a secondary refracted shock (sRS) and a reflected shock (RfS). At 118.0 μs, the interaction between RS1 and RS2 reconfigures into a Type I shock-shock interaction. At 119.2 μs, we observe the crossing of RS1 and RS2 without obvious interference. At 120.0 μs, RS1 reaches the downstream pole, and RS2 merges with other derived wave structures and is no longer distinguishable. At 120.6 μs, RS1 propagates through the downstream slow-fast interface, and the outcomes are a refracted shock (RS3) and reflected rarefaction waves. At the rear of the downstream pole, the sRS catches up with the IS and will collide with its reflection on the axis; this finding is a new explanation of shock focusing in complement with the collision of curved incident shocks [18,19]. Meanwhile, the shocks inside the bubble merge near the downstream pole. At 121.0 μs, after the shock collision, a hot spot with a maximum temperature of approximately 1500 K is detected at the rear of the downstream pole. The shock collision generates two hot jets that propagate upstream and downstream. For the upstream jet inside the bubble, Mach reflection occurs, and the merged shock acts as the secondary incident shock (sIS).

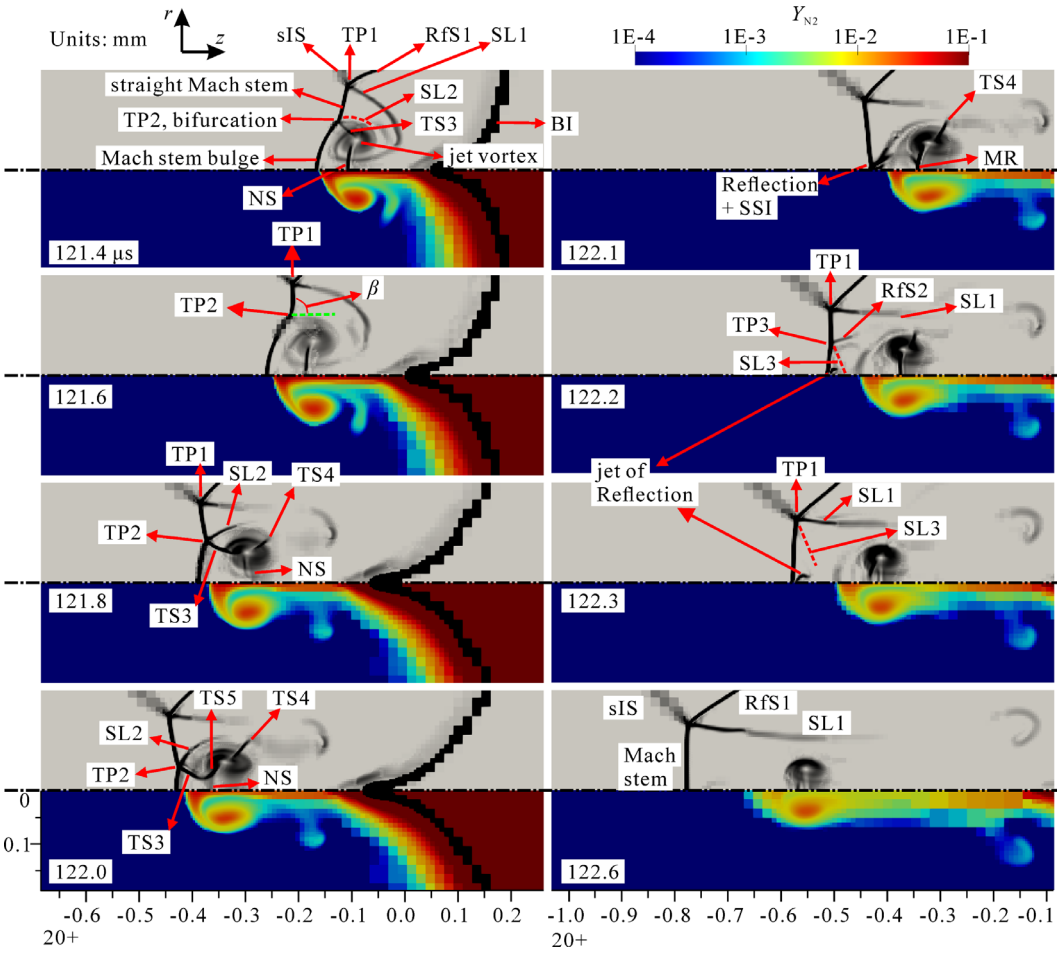

Figure 15. Sequences of numerical schlieren contours (upper regions) and Y_{N2} contours (lower regions) during the Mach reflection transition in the ISBI case from 121.4 to 122.6 μs. MR: Mach reflection, NS: normal shock, SL: slip line, SSI: shock-shock interaction, TP: triple point, TS: transmitted shock. For the meanings of other symbols, please refer to Figure 14.

Figure 15 presents the Mach reflection transition from 121.4 to 122.6 μs. At 121.4 μs, although the main flow feature propagates to the right, the secondary incident shock (sIS) moves to the left. The sIS has a relatively poor resolution because the post-shock temperature is lower than T_{et}, and the local grids are loosely refined. Hornung [19] pointed out that the SFP is indeed the cylindrical shock reflection phenomenon, and the outcome must be Mach reflection because of the Guderley singularity that arises from the cylindrically converging shocks [47]. Therefore, here, we observe a Mach stem, a reflected shock (RfS1), a triple point (TP1), and a slip line (SL1). Moreover, because of the strong backward jet, the Mach stem bifurcates into the upper straight Mach stem and the lower Mach stem bulge with a new triple point (TP2) [48,49]. The Mach stem bulge is weaker than the straight Mach stem. For the flows to be in mechanical equilibrium, a Type III shock-shock interaction occurs at TP2 and generates a transmitted shock (TS3) and a slip line (SL2, the red dashed curve) according to Edney [46]. In

addition, a nearly normal shock (NS) appears inside the jet to match the pressure behind the Mach stem bulge and in the jet flow, and the jet vortex entrains SL1 into the core.

In Figure 15, at 121.6 μs, since the temperature around TP2 drops below T_{et}, the disappearance of TS3 is possibly caused by insufficient grid resolution. Because TP1 travels faster than the Mach stem foot, TP2 gradually lies behind TP1; the inclination of the straight Mach stem, β, increases from a sharp incline (at 121.4 μs) to nearly 90° (at 121.6 μs) and later becomes obtuse. At 121.8 μs, the Type III shock-shock interaction reappears. TS3 further interacts with the normal shock (NS) in the backward jet and produces another transmitted shock (TS4). At 122.0 μs, as TP1 lies more upstream than the Mach stem foot, TP2 and TS3 approach the symmetry axis. A new transmitted shock (TS5) appears as a result of the interaction between TS3 and NS. Meanwhile, the jet vortex alters the local pressure distribution; this alteration reallocates TS4, which is no longer closely related to TS3 and NS. At 122.1 μs, TP2 collides with its reflection on the axis, and TS5 produces a Mach reflection (MR) downstream. During this collision of triple points, the waves connecting to TP2, including the straight Mach stem, TS3, SL2, and the Mach stem bulge, and they all reflect on the axis and cause strong shock-shock interactions. At 122.2 μs, the reflected shock (RfS2) that arises from the triple point collision interacts with the Mach stem and forms a triple point (TP3) and a slip line (SL3, the red dashed line). This reflection also induces a new jet behind the Mach stem. At 122.3 μs, RfS2 reaches SL1, the Mach stem becomes nearly straight, and SL3 now connects to TP1. After 122.3 μs, the new jet no longer affects the Mach stem, and the wave systems transit to a single Mach reflection.

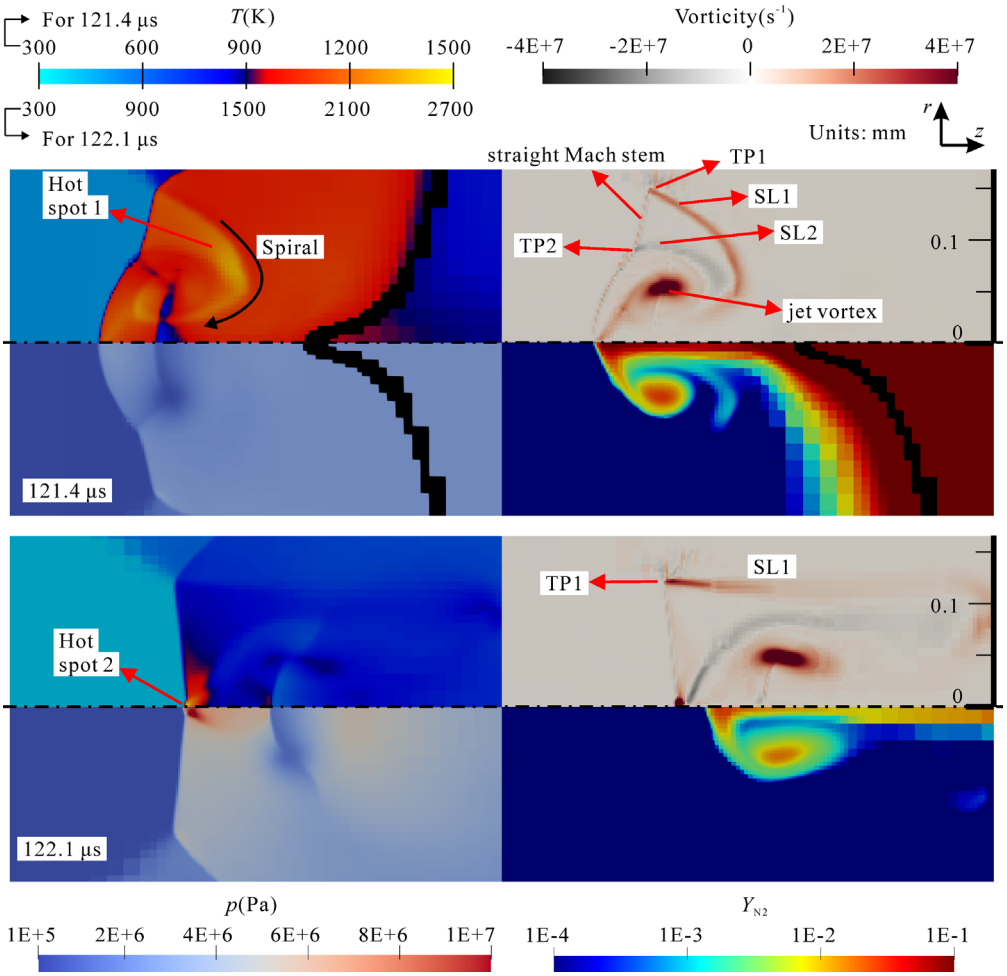

Figure 16. The formations of two hot spots in the ISBI case at 121.4 and 122.1 μs. The contours in each quadrant represent the (I) vorticity, (II) temperature, (III) pressure, and (IV) Y_{N2}. For the meanings of other symbols, please refer to Figure 15.

Figure 16 illustrates the flow fields when two hot spots form in the ISBI case at 121.4 and 122.1 μs. At 121.4 μs, the backward jet propagates into the bubble and induces bifurcated Mach reflection. The jet vortex entrains the mixtures compressed by the straight Mach stem into the vortex core, which converts some kinetic energy into internal energy and further increases the temperature to approximately 1500 K. These form spiral hot spot 1. At 122.1 μs, the triple point collision includes complex shock-shock interactions on the axis, which leads to the formation of hot spot 2 at approximately 2700 K and 100 bar. The importance of this type of hot spot, which originates from the bifurcated Mach reflection and triple point collision, was verified by Bhattacharjee et al. [50] on detonation re-initiation and by Mahmoudi et al. [51] on flame propagation. Further analysis shows that the formation of these hot spots in both the inert and reactive cases are very similar, so the discussions here also apply to RSBI, and these two hot spots are responsible for the ignitions.

The possible causes of the Mach reflection transition are discussed here. Hornung [19] pointed out that Mach reflection with bifurcation is affected by the incident shock strength, reflected angle, and polytropic exponent. As the jet partly consists of lighter N_2, it is very likely that the transition is influenced by the light-heavy refraction across the bubble interface as it changes these factors. This phenomenon should be further investigated using a simple geometry in the future.

4.4 Ignition and failure of DDT

In this section, we discuss two ignitions during the Mach reflection transition and the failure of DDT in the reactive case.

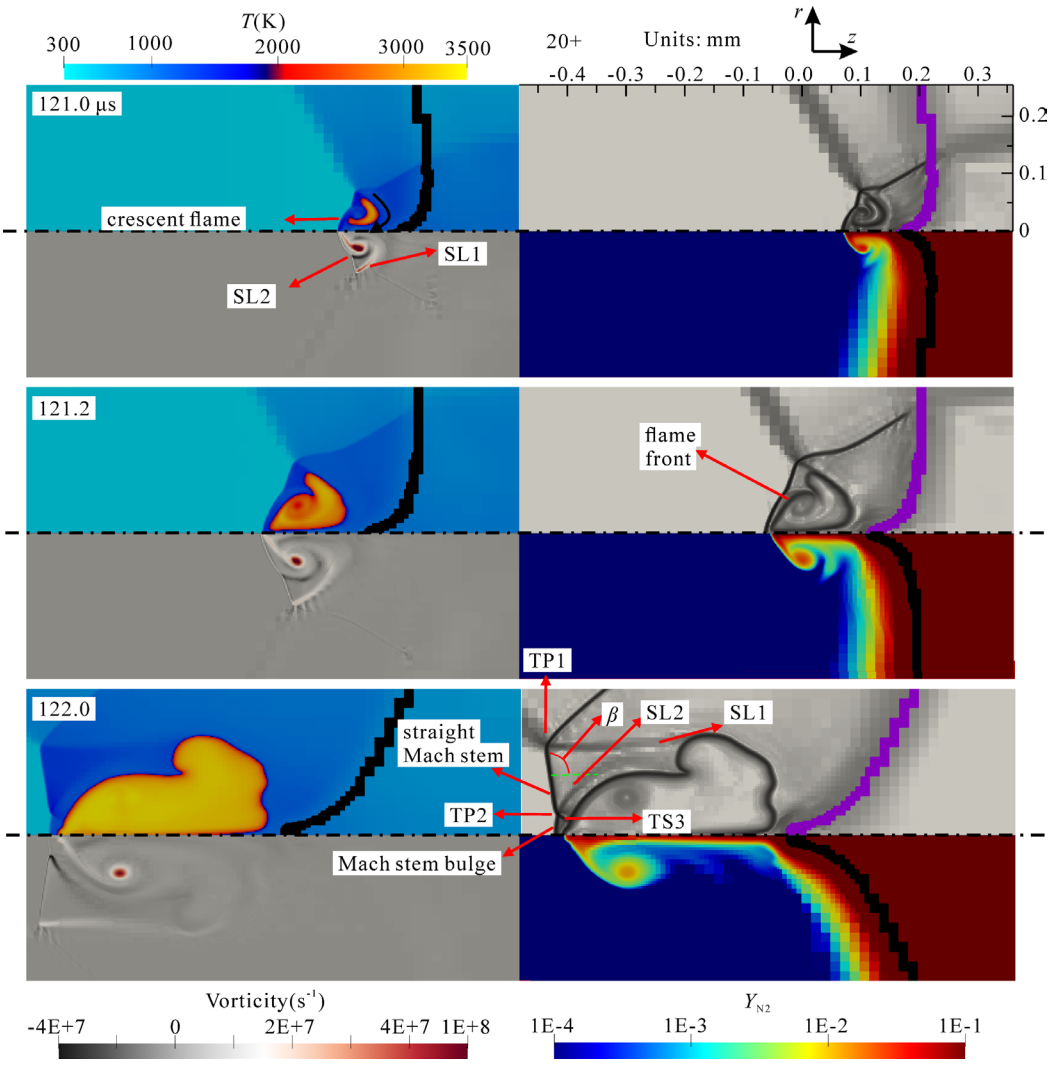

Figure 17. Sequences of the flow fields during the first ignition in the RSBI case from 121.0 to 122.0 μs. The contour in each quadrant represents the (I) enhanced numerical schlieren, (II) temperature, (III) vorticity, and (IV) Y_{N2}. For the meanings of symbols, please refer to Figure 14 and Figure 15.

Figure 17 presents the flow fields during the first ignition from 121.0 to 122.0 μs in the RSBI case. At 121.0 μs, the premixtures are ignited by spiral hot spot 1 in the jet and produce the crescent flame. The backward jet is

attached to the preceding Mach stem, but the flame fronts are decoupled from it. At 121.2 μs, the lower flame front gets entrained into the jet vortex core, and the upper flame front propagates along the slip line toward the straight Mach stem. At 122.0 μs, TP1 lies more upstream than the Mach stem foot, and a Type III shock-shock interaction occurs at TP2. The flame extrudes more horizontally near the axis because of the streamwise jet penetration. The temperature distribution inside the jet vortex is no longer inhomogeneous and implies that the reaction here is almost completed. Until this moment, the bifurcated Mach stem is almost the same as the inert stem. Therefore, the Mach reflection transition will occur in the RSBI case.

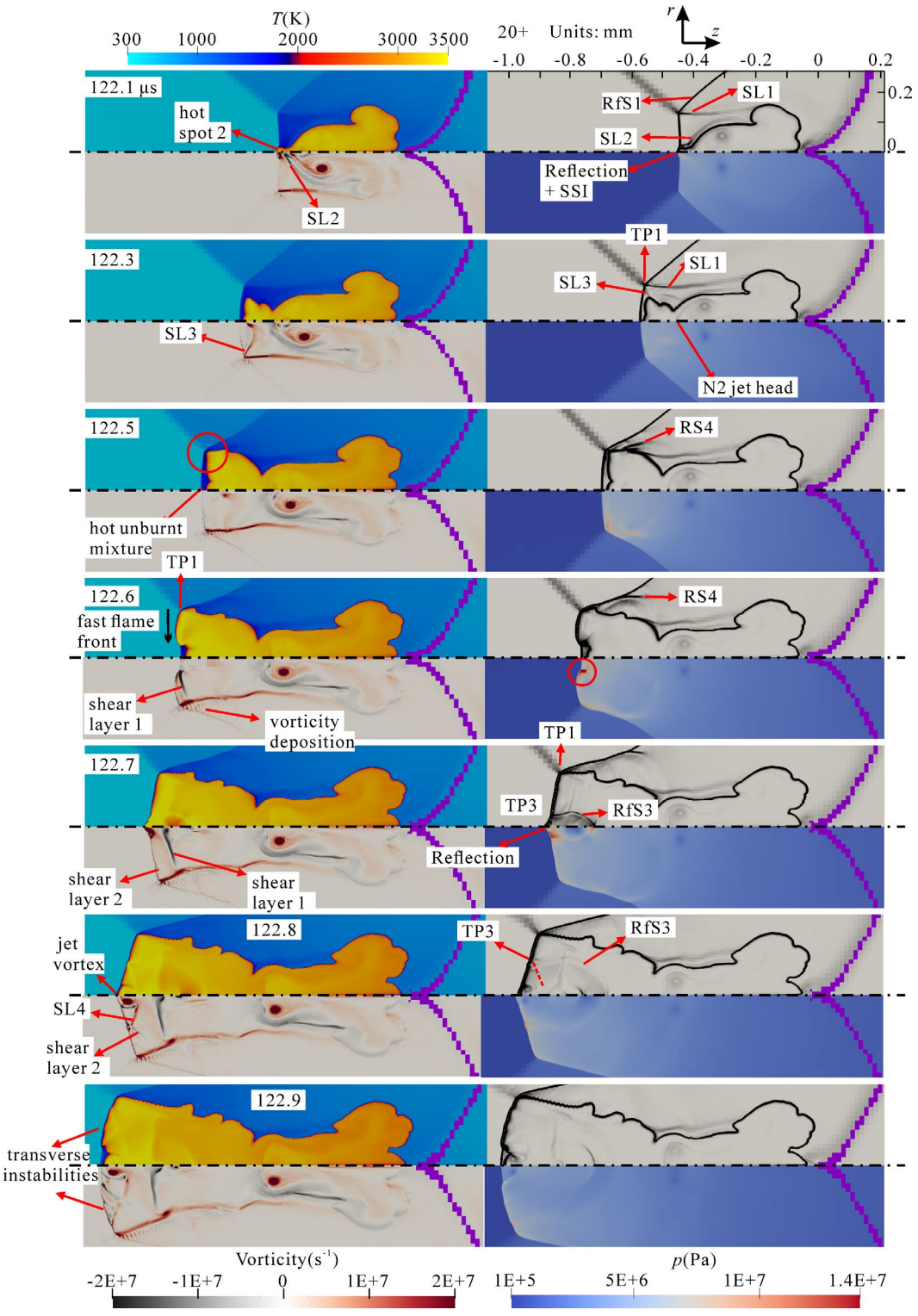

Figure 18. Sequences of the flow fields during the second ignition and failure of DDT in the RSBI case from 122.1 to 122.9 μs. The contours in each quadrant represent the (I) numerical schlieren, (II) temperature, (III) vorticity, and (IV) pressure. For the meanings of symbols, please refer to Figure 14 and Figure 15.

Figure 18 presents the flame development during the second ignition and failure of DDT in the reactive case. At 122.1 μs, the triple point collision produces hot spot 2 which is responsible for the second ignition. Since this collision occurs before the flame affects the flow field, the second ignition is not caused by the earlier jet flame

through the diffusivity mechanism but is more related to the spontaneous ignition. The newborn flame fronts induce a bulge at the Mach stem foot. At 122.2 μs, which is not shown, the bulge interacts with the preceding Mach stem, and the results are a triple point, a reflected shock, and a slip line, and the interaction is similar to the inert case in Figure 15. At 122.3 μs, the reflected shock reaches TP1, SL3 now connects to TP1, and a portion of the newborn flame propagates along SL3 to TP1. The flame fronts are now fully decoupled from the preceding shocks, and the pressure field proves that the flame is deflagration. At 122.5 μs, the flame fronts reach SL1 and produce a refracted shock (RS4). Along SL3, the flame almost reaches TP1. The unburnt mixtures between the flame fronts and Mach stem are hotter than 1500 K. At 122.6 μs, the flame fronts interact with TP1, and this interaction produces a fast combustion wave that travels toward the axis with a speed of approximately 1050 m/s. This fast flame is due to the reactivity gradient in the hot unburnt premixture through the Zeldovich mechanism [52]. The upper portion of the Mach stem experiences a shock-flame interaction and turns into shear layer 1, but the lower portion is still decoupled from the flame. Near TP1, the mixtures between SL1 and RfS1 are ignited and deposit vorticities. From 122.7 to 122.8 μs, the Mach stem overlaps with the flame fronts. The fast combustion wave collides with its reflection on the axis and produces a jet vortex, a triple point (TP3), and a slip line (SL4, the red dashed line in the schlieren contour). The interaction between the flame and TP1 produces a train of weak pressure waves between the leftmost flame fronts and shear layer 1. The averaged pressure ratio across these pressure waves is about 1.02, and the leading wave perturbs the flame front and induces shear layer 2. At 122.8 μs, SL4 collides with shear layer 2, which amplifies the perturbations on the flame front. The Mach stem still overlaps with the flame fronts. At 122.9 μs, transverse instabilities develop on the flame fronts, and the lower portion of the Mach stem becomes decoupled from the flame fronts.

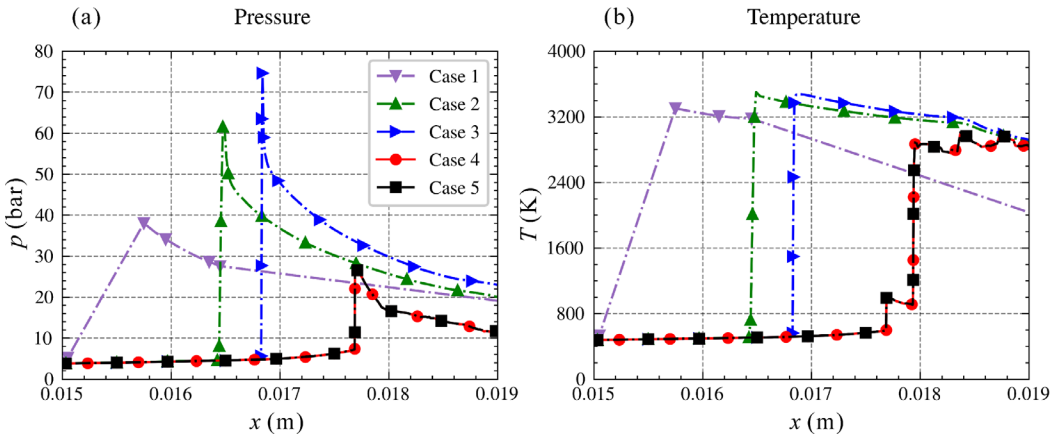

Figure 19. One-dimensional distribution of pressure and temperature along the bubble axis across the upstream frame fronts in the RSBI case from 122.0 to 124.9 μs.

Figure 19 plots the one-dimensional upstream flame structures on the symmetry axis after the second ignition. From 122.0 to 124.9 μs, the second ignition induces complex three-dimensional shock-flame interactions that are responsible for the extreme peak pressure value (such as 140 bar at 122.7 μs). The flame fronts are decoupled from the preceding shock at 123.1 μs but attach to it again at 123.5 μs. Examinations of flow fields show the later attaching, and the formation of a pressure peak can be interpreted similarly to the collision of fast flame fronts on the axis in Figure 18. Since the later peak value is more benign than those at 122.7 μs, no detailed analysis will be presented. Although the flame fronts tend to accelerate, the DDT process eventually fails. The Mach stem is fully decoupled from the flame, and stable deflagration is maintained after 124.3 μs.

The influences of combustion on compression wave structures are also worth discussing. At 121.2 μs, the flame in the hot spiral alters the local sound speed, which destroys the normal shock wave in the backward jet and the later complex shock system shown in Figure 15 at 121.8 μs. Additionally, the TS3 from the Mach stem bifurcation is damped by the near flame front. At 122.1 μs, the downstream Mach reflection of TS5 disappears in the hot jet. After 122.1 μs, the second ignition and fast combustion wave strongly influence the Mach reflection structure by interfering with TP1, SL1, and the preceding Mach stem.

The flame instabilities are caused by the shock-flame interactions or slip-line-flame interactions. In Figure 18, at 122.3 μs, the flame fronts of the second ignition are perturbed by SL3. After the flame front interacts with SL1, at 122.6 μs, a corrugated flame with two sets of peak and valley structures becomes apparent. At 122.7 and 122.8 μs, these corrugated flame fronts are further perturbed by the shear flow and baroclinic torque caused by the RMI effects. The small-scale instabilities on the flame near TP1 are possibly numerical and originate from using rectangular grids to approximate the curved flame front, as suggested by Shen and Parsani [53]. At 122.9 μs, significant transverse instabilities are present on the leftmost flame fronts. These instabilities are due to the interaction between flame fronts and transverse waves, including RfS3 and weak pressure waves, as a result of the RMI effects.

5. Concluding remarks

We numerically study the low-Mach-number (M = 1.34) RSBI in Haehn et al.'s experiment [1,13] using an AMR method and a pressure-dependent comprehensive H_2/O_2 mechanism [36]. Our combustion solver is based on a novel AMR framework and is accurate for RSBI studies. Extra AMR strategies based on an empirical threshold of ignition/flame temperature are proposed and effectively refine the hydrodynamic or chemical discontinuities separately. The grid-convergence test shows that the convergent result is deflagration, and coarse

grids lead to unphysical detonation. The RMI dominates the SBI development. For this heavy bubble case, shock focusing occurs at the rear of the bubble and induces ignition. The deflagration waves increase the transverse bubble diameter and suppress the secondary interfacial KHI structures and upstream jet. We successfully reproduce the experimental bubble morphology and chemiluminescence images, including the bubble length scale, primary and secondary vortices, flame shape, and speed of the flame fronts. The fuel consumption rate is nonmonotonic and is explained by unsteady flame propagation and suppression by interfacial mixing. Deviations possibly arise from the experimental insufficiency in detecting early ignition and may also be related to the neglect of the soap films in our modeling. The total vorticity is not greatly affected by the combustion until 470 μs because of the negative vorticities deposited on the flame fronts. In contrast, combustion strongly promotes the mixing of SBI. In this simulation, the thermal effects of combustion increase the overall mixing by approximately 150% in which 88% of the growth is due to the thermal effects on diffusivity and 12% is related to the species gradient and interfacial area. In addition to traditional shock-focusing explanations, we consider the influence of secondary refracted shock. Mach reflection occurs during shock focusing and becomes bifurcated because of the strong backward jet. Later, this Mach reflection transitions from the bifurcated type to the single type, and this transition is related to wave refraction at the leeward interface. The Mach reflection transition causes two ignitions. The first occurs in the spiral hot spot entrained by the jet vortex, and the flame is a deflagration. The second arises from the hot spot caused by the triple point collision, and the newborn flame is a deflagration in the beginning but tends to transition to a detonation after interaction with the Mach reflection wave structures. The shock-flame interactions accelerate the flame fronts once to approximately 1050 m/s. Finally, the flame fronts are decoupled from the preceding shocks, and the stable combustion mode is deflagration. The reflected wave and weak pressure waves deposit vorticities and lead to transverse instabilities on the flame fronts because of the RMI effects.

Acknowledgments

This work was supported by the Natural Science Foundation of China (nos 11772284 and 12002102) and Hong Kong Research Grants Council (no. 15207420). The authors are also grateful to the National Supercomputer Center in Tianjin for providing the computational resource.

Appendix

A.1 Molecular properties of the species in this study

Table A-1. Molecular properties of all species in this study

Species	$(\varepsilon/k)_i$	σ_i	MW_i(g/mol)
H	541.572	1.530	1.00794
H_2	304.690	2.190	2.01588
H_2O	637.056	2.943	18.01528
H_2O_2	1361.148	3.179	34.0147
HO_2	963.003	3.129	33.00677
N_2	97.839	3.610	28.0134
O	235.686	2.485	15.9994
O_2	676.424	3.069	31.9988
OH	514.598	2.582	17.00734
Xe	282.290	3.8924	131.293

All molecular properties in Table A-1 can be found in Jasper et al. [54], Jasper and Miller [55], and Chapman et al. [56].

A.2 Thermodynamic model

The equation of state for a chemically reacting mixture composed of thermally perfect gases is given by

$$p = \sum_{i=1}^{n_s} \rho_i \frac{R_u}{MW_i} T \tag{22}$$

where R_u is the universal gas constant and MW_i is the species molecular weight.

The total energy per unit volume of the mixture is defined as

$$E = \sum_{i=1}^{n_s} \rho_i \left(h_i - \frac{R_u}{MW_i} T \right) + \frac{1}{2} \rho \left(u^2 + v^2 \right) \tag{23}$$

where the species enthalpy is evaluated from curve fits of the form

$$\frac{h_i(T)}{R_i T} = -a_{i,1} T^{-2} + a_{i,2} \frac{\ln T}{T} + a_{i,3} + a_{i,4} \frac{T}{2} + a_{i,5} \frac{T^2}{3} + a_{i,6} \frac{T^3}{4} + a_{i,7} \frac{T^4}{5} + \frac{b_{i,1}}{T} \tag{24}$$

The species isobaric heat capacity $C_{p,i}$ and entropy S_i are evaluated similarly. The coefficients $a_{i,k}$ and $b_{i,1}$ are obtained from the NASA thermochemical polynomial data [57].

A.3 Transport properties

The transport properties of the mixture are calculated using Wilke's mixing rule:

$$\mu = \sum_{i=1}^{n_s} \frac{X_i}{\phi_i} \mu_i \tag{25}$$

$$\kappa = \sum_{i=1}^{n_s} \frac{X_i}{\phi_i} \kappa_i \tag{26}$$

where X_i is the species molar fraction, and the term ϕ_i is defined as

$$\phi_i = \sum_{m=1}^{n_s} \frac{X_m \left\{ 1 + \sqrt{\frac{\mu_i}{\mu_m}} \left(\frac{MW_m}{MW_i} \right)^{1/4} \right\}^2}{\sqrt{8\left(1 + \frac{MW_i}{MW_m} \right)}} \tag{27}$$

The viscous coefficient μ_i of each species is calculated using the Chapman-Enskog model [56]

$$\mu_i = 2.6693 \cdot 10^{-6} \frac{\sqrt{MW_i T}}{\Omega_{\mu,i} \sigma_i^2} \tag{28}$$

where σ_i is the molecular collision diameter, and the collision integral for viscosity is defined as in Ref. [58]

$$\Omega_{\mu,i} = A(T_i^*)^B + C\exp(DT_i^*) + E\exp(FT_i^*) \tag{29}$$

The parameters are A = 1.16145, B = –0.14874, C = 0.52487, D = –0.7732, E = 2.16178, F = –2.43787, and $T_i^* = T / (\varepsilon / k)_i$ using the Lennard-Jones energy parameter $(\varepsilon / k)_i$ for the i_{th} specie. Table A-1 lists the molecular properties of all species in this study.

The thermal conductivity κ_i of each species is calculated using Eucken's relation [59],

$$\kappa_i = \left(C_{p,i} + \frac{5}{4} \frac{R_u}{MW_i} \right) \cdot \mu_i \tag{30}$$

and the diffusivity D_i of each species is modeled as

$$D_i = (1 - X_i) \left(\sum_{m \neq i}^{n_s} \frac{X_m}{D_{im}} \right)^{-1} \tag{31}$$

The binary diffusion coefficient is calculated using the constitutive empirical law as

$$D_{ij} = \frac{0.0266}{\Omega_{D,ij}} \frac{T^{3/2}}{p\sqrt{M_{ij}}\sigma_{ij}^2} \tag{32}$$

where M_{ij} is the equivalent molecular mass of the binary mixture defined as

$$M_{ij} = \frac{2}{\frac{1}{M_i} + \frac{1}{M_j}} \tag{33}$$

σ_{ij} is the averaged collision diameter, which is expressed as

$$\sigma_{ij} = \frac{\sigma_i + \sigma_j}{2} \tag{34}$$

and the collision integral for binary diffusion is defined as

$$\Omega_{D,ij} = A^*(T_{ij}^*)^{B^*} + C^*\exp(D^*T_{ij}^*) + E^*\exp(F^*T_{ij}^*) + G^*\exp(H^*T_{ij}^*) \tag{35}$$

where $A^* = 1.06036$, $B^* = -0.1561$, $C^* = 0.19300$, $D^* = -0.47635$, $E^* = 1.03587$, $F^* = -1.52996$, $G^* = 1.76474$, and $H^* = -3.89411$. $T_{ij} = T / T_{\varepsilon_{ij}}$, in which $T_{\varepsilon_{ij}}$ is defined using the Lennard-Jones energy parameter [7]

$$T_{\varepsilon_{ij}} = \sqrt{\left(\frac{\varepsilon}{k}\right)_i \left(\frac{\varepsilon}{k}\right)_j} \tag{36}$$

A.4 Chemical model

Detailed chemical mechanisms are implemented in this work. The general formula for a chemical mechanism with n_r elementary reactions can be expressed as

$$\sum_{i=1}^{n_s} \nu_{m,i}^f X_i \longleftrightarrow \sum_{i=1}^{n_s} \nu_{m,i}^b X_i, m = 1,...,n_r \tag{37}$$

where $\nu_{m,i}^f$ and $\nu_{m,i}^b$ are the stoichiometric coefficients of the reactants and products of each reaction. The net mass production rate for each species is calculated as

$$\omega_i = MW_i \sum_{m=1}^{n_r} \left(\nu_{m,i}^b - \nu_{m,i}^f\right) \left[k_{f,m} \prod_{j=1}^{n_s} \left(\frac{\rho_j}{MW_j}\right)^{\nu_{m,j}^f} - k_{b,m} \prod_{j=1}^{n_s} \left(\frac{\rho_j}{MW_j}\right)^{\nu_{m,j}^b} \right] \tag{38}$$

where $k_{f,m}$ and $k_{b,m}$ are forward and backward reaction rate constants, respectively, and are given by

$$k_{f,m} = A_{f,m} T^{B_{f,m}} \exp\left(-\frac{E_{f,m}}{R_u T}\right) \tag{39}$$

$$k_{b,m} = \frac{k_{f,m}}{K_{c,m}} \tag{40}$$

where $A_{f,m}$ is the pre-exponential factor, $B_{f,m}$ is the temperature exponential factor, and $E_{f,m}$ is the activation energy. $K_{c,m}$ is the equilibrium constant of each reaction, which is expressed as

$$K_{c,m} = \exp\left(-\frac{\Delta G_m^0}{R_u T}\right) \left(\frac{R_u T}{p_{\text{atm}}}\right)^{\sum_i (\nu_{r,i}^f - \nu_{r,i}^b)} \tag{41}$$

where ΔG_m^0 is the change of Gibbs free energy and $p_{\text{atm}} = 1$ atm.

References

[1] N. Haehn, D. Ranjan, C. Weber, J. Oakley, D. Rothamer, R. Bonazza, Reacting shock bubble interaction, Combustion and Flame. 159 (2012) 1339–1350. https://doi.org/10.1016/j.combustflame.2011.10.015.

[2] M. Brouillette, the Richtmyer-Meshkov Instability, Annual Review of Fluid Mechanics. 34 (2002) 445–468. https://doi.org/10.1146/annurev.fluid.34.090101.162238.

[3] N.J. Zabusky, VORTEX PARADIGM FOR ACCELERATED INHOMOGENEOUS FLOWS: Visiometrics for the Rayleigh-Taylor and Richtmyer-Meshkov Environments, Annu. Rev. Fluid Mech. 31 (1999) 495–536. https://doi.org/10.1146/annurev.fluid.31.1.495.

[4] Y. Zhou, T.T. Clark, D.S. Clark, S. Gail Glendinning, M. Aaron Skinner, C.M. Huntington, O.A. Hurricane, A.M. Dimits, B.A. Remington, Turbulent mixing and transition criteria of flows induced by hydrodynamic instabilities, Physics of Plasmas. 26 (2019) 080901. https://doi.org/10.1063/1.5088745.

[5] R.D. Richtmyer, Taylor instability in shock acceleration of compressible fluids, Communications on Pure and Applied Mathematics. 13 (1960) 297–319. https://doi.org/10.1002/cpa.3160130207.

[6] E. Meshkov, Instability of the interface of two gases accelerated by a shock wave, Fluid Dynamics. 4 (1969) 101–104.

[7] D. Ranjan, J. Oakley, R. Bonazza, Shock-Bubble Interactions, Annual Review of Fluid Mechanics. 43 (2011) 117–140. https://doi.org/10.1146/annurev-fluid-122109-160744.

[8] J.-F. Haas, B. Sturtevant, Interaction of weak shock waves with cylindrical and spherical gas inhomogeneities, J. Fluid Mech. 181 (1987) 41. https://doi.org/10.1017/S0022112087002003.

[9] J.W. Jacobs, Shock-induced mixing of a light-gas cylinder, J. Fluid Mech. 234 (1992) 629. https://doi.org/10.1017/S0022112092000946.

[10] C. Tomkins, S. Kumar, G. Orlicz, K. Prestridge, An experimental investigation of mixing mechanisms in shock-accelerated flow, Journal of Fluid Mechanics. 611 (2008) 131–150. https://doi.org/10.1017/S0022112008002723.

[11] J.H.J. Niederhaus, J.A. Greenough, J.G. Oakley, D. Ranjan, M.H. Anderson, R. Bonazza, A computational parameter study for the three-dimensional shock–bubble interaction, Journal of Fluid Mechanics. 594 (2008) 85–124. https://doi.org/10.1017/S0022112007008749.

[12] N. Haehn, C. Weber, J. Oakley, M. Anderson, D. Rothamer, D. Ranjan, R. Bonazza, Experimental Shock-Initiated Combustion of a Spherical Density Inhomogeneity, in: K. Kontis (Ed.), 28th International Symposium on Shock Waves, Springer Berlin Heidelberg, Berlin, Heidelberg, 2012: pp. 359–364. https://doi.org/10.1007/978-3-642-25685-1_54.

[13] N.S. Haehn, Experimental Investigation of the Reactive Shock-bubble Interaction, PhD Thesis, The University of Wisconsin-Madison, 2012.

[14] F. Diegelmann, V. Tritschler, S. Hickel, N. Adams, On the pressure dependence of ignition and mixing in two-dimensional reactive shock-bubble interaction, Combustion and Flame. 163 (2016) 414–426. https://doi.org/10.1016/j.combustflame.2015.10.016.

[15] F. Diegelmann, S. Hickel, N.A. Adams, Shock Mach number influence on reaction wave types and mixing in reactive shock–bubble interaction, Combustion and Flame. 174 (2016) 85–99. https://doi.org/10.1016/j.combustflame.2016.09.014.

[16] F. Diegelmann, S. Hickel, N.A. Adams, Three-dimensional reacting shock–bubble interaction, Combustion and Flame. 181 (2017) 300–314. https://doi.org/10.1016/j.combustflame.2017.03.026.

[17] S. Gs, G.V. Candler, Large eddy simulations of reacting shock-bubble interaction, in: Sonderforschungsbereich/Transregio 40-Summer Program Report 2015, 2017: p. 14.

[18] N. Zabusky, S. Zeng, Shock cavity implosion morphologies and vortical projectile generation in axisymmetric shock–spherical fast/slow bubble interactions, Journal of Fluid Mechanics. 362 (1998) 327–346.

[19] H.G. Hornung, Oblique shock reflection from an axis of symmetry, J. Fluid Mech. 409 (2000) 1–12. https://doi.org/10.1017/S0022112099007831.

[20] E.S. Oran, J.W. Weber, E.I. Stefaniw, M.H. Lefebvre, J.D. Anderson, A Numerical Study of a Two-Dimensional H2-O2-Ar Detonation Using a Detailed Chemical Reaction Model, Combustion and Flame. 113 (1998) 147–163. https://doi.org/10.1016/S0010-2180(97)00218-6.

[21] F. Sharpe, S.A.E.G. Sharpe, Two-dimensional numerical simulations of idealized detonations, Proc. R. Soc. Lond. A. 456 (2000) 2081–2100. https://doi.org/10.1098/rspa.2000.0603.

[22] G.J. Sharpe, Transverse waves in numerical simulations of cellular detonations, J. Fluid Mech. 447 (2001) 31–51. https://doi.org/10.1017/S0022112001005535.

[23] Y. Mahmoudi, K. Mazaheri, High resolution numerical simulation of the structure of 2-D gaseous detonations, Proceedings of the Combustion Institute. 33 (2011) 2187–2194. https://doi.org/10.1016/j.proci.2010.07.083.

[24] K. Mazaheri, Y. Mahmoudi, M.I. Radulescu, Diffusion and hydrodynamic instabilities in gaseous detonations, Combustion and Flame. 159 (2012) 2138–2154. https://doi.org/10.1016/j.combustflame.2012.01.024.
[25] E.S. Oran, V.N. Gamezo, Origins of the deflagration-to-detonation transition in gas-phase combustion, Combustion and Flame. 148 (2007) 4–47. https://doi.org/10.1016/j.combustflame.2006.07.010.
[26] K. Schmidmayer, F. Petitpas, S. Le Martelot, É. Daniel, ECOGEN: An open-source tool for multiphase, compressible, multiphysics flows, Computer Physics Communications. 251 (2020) 107093. https://doi.org/10.1016/j.cpc.2019.107093.
[27] A.M. Khokhlov, Fully Threaded Tree Algorithms for Adaptive Refinement Fluid Dynamics Simulations, Journal of Computational Physics. 143 (1998) 519–543. https://doi.org/10.1006/jcph.1998.9998.
[28] K. Schmidmayer, F. Petitpas, E. Daniel, Adaptive Mesh Refinement algorithm based on dual trees for cells and faces for multiphase compressible flows, Journal of Computational Physics. 388 (2019) 252–278. https://doi.org/10.1016/j.jcp.2019.03.011.
[29] E.F. Toro, Riemann solvers and numerical methods for fluid dynamics: a practical introduction, 3rd ed, Springer, Dordrecht ; New York, 2009.
[30] B. Van Leer, Towards the ultimate conservative difference scheme. II. Monotonicity and conservation combined in a second-order scheme, Journal of Computational Physics. 14 (1974) 361–370.
[31] A. Syrakos, S. Varchanis, Y. Dimakopoulos, A. Goulas, J. Tsamopoulos, A critical analysis of some popular methods for the discretisation of the gradient operator in finite volume methods, Physics of Fluids. 29 (2017) 127103. https://doi.org/10.1063/1.4997682.
[32] D.G. Goodwin, R.L. Speth, H.K. Moffat, B.W. Weber, Cantera: An Object-oriented Software Toolkit for Chemical Kinetics, Thermodynamics, and Transport Processes, 2018. https://doi.org/10.5281/zenodo.1174508.
[33] J. Williamson, Low-storage runge-kutta schemes, Journal of Computational Physics. 35 (1980) 48–56.
[34] A.M. Khokhlov, E.S. Oran, A.Y. Chtchelkanova, J.C. Wheeler, Interaction of a shock with a sinusoidally perturbed flame, Combustion and Flame. 117 (1999) 99–116.
[35] G. Billet, V. Giovangigli, G. de Gassowski, Impact of volume viscosity on a shock–hydrogen-bubble interaction, Combustion Theory and Modelling. 12 (2008) 221–248. https://doi.org/10.1080/13647830701545875.
[36] M. Ó Conaire, H.J. Curran, J.M. Simmie, W.J. Pitz, C.K. Westbrook, A Comprehensive Modeling Study of Hydrogen Oxidation, International Journal of Chemical Kinetics. 36 (2004) 603–622. https://doi.org/10.1002/kin.20036.
[37] E. Petersen, D. Davidson, M. Röhrig, R. Hanson, High-pressure shock-tube measurements of ignition times in stoichiometric H2/O2/Ar mixtures, in: Proceedings of the 20th International Symposium on Shock Waves, 1996: pp. 941–946.
[38] K. Hughes, T. Turányi, A. Clague, M. Pilling, Development and testing of a comprehensive chemical mechanism for the oxidation of methane, International Journal of Chemical Kinetics. 33 (2001) 513–538.
[39] C.J. Jachimowski, An analytical study of the hydrogen-air reaction mechanism with application to scramjet combustion, (1988).
[40] F. Williams, others, Chemical-Kinetic Mechanisms for Combustion Applications, Mechanical and Aerospace Engineering (Combustion Research), University of California at San Diego. (2012). https://web.eng.ucsd.edu/mae/groups/combustion/mechanism.html.
[41] L. Massa, P. Jha, Linear analysis of the Richtmyer-Meshkov instability in shock-flame interactions, Phys. Fluids. 24 (2012) 056101. https://doi.org/10.1063/1.4719153.
[42] D. Ranjan, J.H.J. Niederhaus, J.G. Oakley, M.H. Anderson, J.A. Greenough, R. Bonazza, Experimental and numerical investigation of shock-induced distortion of a spherical gas inhomogeneity, Physica Scripta. T132 (2008) 014020. https://doi.org/10.1088/0031-8949/2008/T132/014020.
[43] R. Mével, S. Pichon, L. Catoire, N. Chaumeix, C.-E. Paillard, J.E. Shepherd, Dynamics of excited hydroxyl radicals in hydrogen-based mixtures behind reflected shock waves, Proceedings of the Combustion Institute. 34 (2013) 677–684. https://doi.org/10.1016/j.proci.2012.06.151.
[44] F. Takahashi, Extinguishment of diffusion flames around a cylinder in a coaxial air stream with dilution or water mist, Proceedings of the Combustion Institute. (2009) 9.
[45] S. Sarkar, A. Mukhopadhyay, S. Sen, The effects of steam and water spray on NO formation in a methane–air counterflow diffusion flame, Combustion Theory and Modelling. (2021) 1–28. https://doi.org/10.1080/13647830.2021.1905880.
[46] B. Edney, Anomalous Heat Transfer and Pressure Distributions on Blunt Bodies at Hypersonic Speeds in the Presence of an Impinging Shock., Flygtekniska Forsoksanstalten, Stockholm (Sweden), 1968.
[47] G.B. Whitham, Linear and nonlinear waves, Wiley, New York Chichester Weinheim, 1999.
[48] B.W. Skews, N. Menon, M. Bredin, E.V. Timofeev, An experiment on imploding conical shock waves, Shock Waves. 11 (2002) 323–326. https://doi.org/10.1007/s001930100115.

[49] L.F. Henderson, E.I. Vasilev, G. Ben-Dor, T. Elperin, The wall-jetting effect in Mach reflection: theoretical consideration and numerical investigation, J. Fluid Mech. 479 (2003) 259–286. https://doi.org/10.1017/S0022112002003518.
[50] R.R. Bhattacharjee, S.S.M. Lau-Chapdelaine, G. Maines, L. Maley, M.I. Radulescu, Detonation re-initiation mechanism following the Mach reflection of a quenched detonation, Proceedings of the Combustion Institute. 34 (2013) 1893–1901. https://doi.org/10.1016/j.proci.2012.07.063.
[51] Y. Mahmoudi, K. Mazaheri, Triple Point Collision and Hot Spots in Detonations with Regular Structure, Combustion Science and Technology. 184 (2012) 1135–1151. https://doi.org/10.1080/00102202.2012.664004.
[52] Y. Zeldovich, Regime classification of an exothermic reaction with nonuniform initial conditions, Combustion and Flame. 39 (1980) 211–214. https://doi.org/10.1016/0010-2180(80)90017-6.
[53] H. Shen, M. Parsani, The role of multidimensional instabilities in direct initiation of gaseous detonations in free space, Journal of Fluid Mechanics. 813 (2017). https://doi.org/10.1017/jfm.2017.5.
[54] A.W. Jasper, E. Kamarchik, J.A. Miller, S.J. Klippenstein, First-principles binary diffusion coefficients for H, H_2, and four normal alkanes + N_2, The Journal of Chemical Physics. 141 (2014) 124313. https://doi.org/10.1063/1.4896368.
[55] A.W. Jasper, J.A. Miller, Lennard–Jones parameters for combustion and chemical kinetics modeling from full-dimensional intermolecular potentials, Combustion and Flame. 161 (2014) 101–110. https://doi.org/10.1016/j.combustflame.2013.08.004.
[56] S. Chapman, T.G. Cowling, D. Burnett, The mathematical theory of non-uniform gases: an account of the kinetic theory of viscosity, thermal conduction and diffusion in gases, Cambridge university press, 1990.
[57] B.J. McBride, M.J. Zehe, S. Gordon, NASA Glenn Coefficients for Calculating Thermodynamic Properties of Individual Species, (2002) 297.
[58] P.D. Neufeld, A. Janzen, R. Aziz, Empirical equations to calculate 16 of the transport collision integrals $\Omega^{(l,s)*}$ for the Lennard-Jones (12–6) potential, The Journal of Chemical Physics. 57 (1972) 1100–1102.
[59] R.J. Kee, M.E. Coltrin, P. Glarborg, Chemically reacting flow: theory and practice, Wiley-Interscience, Hoboken, N.J, 2003.